PHYSICAL REVIEW FLUIDS **2**, 124004 (2017)

Hierarchical micro- and nanofabrication by pattern-directed contact instabilities of thin viscoelastic films

Abir Ghosh,[1] Dipankar Bandyopadhyay,[2,3,*] Jayati Sarkar,[4] and Ashutosh Sharma[1,†]
[1] *Department of Chemical Engineering, Indian Institute of Technology Kanpur, Uttar Pradesh 208016, India*
[2] *Department of Chemical Engineering, Indian Institute of Technology Guwahati, Assam 781039, India*
[3] *Centre for Nanotechnology, Indian Institute of Technology Guwahati, Assam 781039, India*
[4] *Department of Chemical Engineering, Indian Institute of Technology Delhi, New Delhi 110016, India*

(Received 9 April 2017; published 20 December 2017)

A surface of a thin viscoelastic film forms spinodal patterns when brought in contact proximity of another surface due to the dominance of destabilizing intermolecular interaction over the stabilizing elastic and surface tension forces. In this study, we theoretically explore such contact instabilities of a thin viscoelastic film, wherein the patterns generated on the surface of the film is developed with the help of a contactor decorated with periodic physical, chemical, and physicochemical features on the surface. The nonlinear analysis shown here considers the movement of the patterned contactor during the adhesion and debonding processes, which is unlike most of the previous works where the contactor is considered to be stationary. The simulations reveal that the amplitude and periodicity of the patterns decorated on the contactor together with the contactor speed can be the key parameters to stimulate pattern formation on the film surface alongside causing changeover of the various modes of debonding of the surfaces. In particular, the ratio of the elastic to viscous compliances of the film is found to play a critical role to stimulate the changeover of the modes from catastrophic to peeling or coalescence. The study uncovers that a higher wettability contrast across the patterned contactor leads to the catastrophic collapse of the patterns decorated on the film surface when the contactor debonds at a moderate speed. In comparison, a moderately high wettability contrast alongside a faster withdrawal speed of the contactor results in the gradual peeling of columns during the debonding cycle. Remarkably, a higher withdrawal speed of the contactor from the film-proximity can increase the aspect ratio of the patterns fabricated on the film surface to about fourfold during the peeling mode of debonding. The results show the importance of the usage of patterned contactors, their controlled movement, and extent of elastic to viscous compliance ratio of the film for the improvement of the aspect ratio of the patterns developed using the elastic contact lithography of the thin viscoelastic films. The simulations also reveal the possibilities of the fabrication of biomimetic micro- or nanostructures such as columns, holes, cavities, or a combination of these patterns with large-area ordering employing the patterned contactors. A few example cases are shown to highlight the capacity of the proposed methodology for the fabrication of higher aspect ratio hierarchical micro- or nanostructures.

DOI: 10.1103/PhysRevFluids.2.124004

I. INTRODUCTION

Mesoscale surface patterns with large-area ordering offer remarkably high surface-to-volume ratio useful for diverse modern-day applications, such as solar or fuel cells [1], pressure sensitive adhesives [2–11], electronic devices [12], microfluidic applications [13,14], optoelectronics [15], artificial tissues [16], energy harvesting and storage [17,18], superhydrophobic [19,20], or

---

[*] dipban@iitg.ernet.in

[†] ashutos@iitk.ac.in

self-cleaning surfaces [21,22]. Thus, in the past few decades, a number of top-down or bottom-up micro- or nanofabrication techniques have been invented for the large-scale manufacturing of patterned surfaces [23–25]. In this regard, of late, the self-organizing elastic contact lithography (ECL) is found to be a simple and cost-effective alternative for fabricating micro- or nanoscale patterns on the soft polymeric films [26–37]. The ECL exploits the contact instabilities of the thin films originating from the intersurface adhesive interaction between a soft polymeric surface and a rigid approaching contactor to generate patterns. Presently, the major challenges of the commercial viability of the ECL have been the development of high-density patterns with higher aspect ratio [31,38]. The studies on the ECL are also scientifically important because they are the model prototypes to study adhesion-debonding [39,40], tack experiments [5,41], heterogeneous nucleation [42,43], confinement-effects [4,5,7], and crack propagation [5]. Recent experimental [40,44,45] and theoretical [46,47] works reveal that the use of patterned contactor helps in imposing a large area ordering to the surface patterns developed by ECL. In this direction, an extensive exploration is in progress to identify the pathways to develop high-density and high-aspect-ratio patterns on soft polymeric films employing ECL.

The contact instabilities on the surface of a thin polymeric film manifest when the destabilizing van der Waals forces originating from the interaction between the contactor and film overcome the restoring surface tension force at the polymer-air free surface and the bulk elasticity of the film [34,35]. The length scale (λ) of these instabilities is found to be independent of the characteristics of the long-range intermolecular interactions. Interestingly, the length scales of the contact instabilities show a direct linear correspondence with the film thickness (h), $\lambda \sim nh$ [34,35], and the short-wave nature of the instability prevails ($n \sim 3$) for the films having thicknesses more than a few microns. In contrast, the length scale of the contact instability shifts towards the longer wavelength regime ($n \gg 3$) owing to the dominance of the surface tension force [38] or elastocapillary effects [48]. Importantly, the contact instabilities can develop varieties of complex surface morphologies with the very high surface-to-volume ratios, such as the bicontinuous labyrinths, columns, channels, cavities, droplets, and holes, among others [38,49]. The size and periodicity of these patterns can easily be modulated by altering the various thermodynamic parameters, such as the strength of the intermolecular interaction or the surface energy [46,50–52]. Further, the kinetic parameters, such as the approach or withdrawal speed of the contactor, elastic or viscous compliances of the film, and the strength of the external noise, are also found to play decisive roles while the surface patterns are formed [52].

A number of recent theoretical [53] and experimental [45] works show the pathways to fabricate large-area-ordered micro- or nanostructures using the contact instabilities of thin viscoelastic films. These studies discuss the possible modes of debonding, such as the catastrophic, peeling, or the coalescence. Further, they have shown the importance of the speed of contactor during approach and withdrawal, the ratio of the viscous-to-elastic compliance (compliance ratio, C_R) of the film, and patterns decorated on the contactor. A very recent work has shown a threefold increase in the aspect ratio of the patterns on the soft elastic bilayers when the contact instabilities are engendered by the physically patterned contactors [45]. However, there are very few studies that address the issues associated with the improvement in the aspect ratio and density of the patterns originating from the contact instabilities of thin viscoelastic films.

Herein, with the help of 3D nonlinear long-wave simulations [53–56], we investigate these issues in detail. We assume that the film to be a linear zero-frequency viscoelastic [53,55,56] solid with permanent storage and loss moduli. We employ topographically (physically), chemically, or physicochemically patterned contactors with periodic wettability contrast to develop ordered surface patterns on the film through variable intersurface adhesive interaction. We also impose a finite speed to the contactor to mimic the experimental situations associated with the contact instabilities of thin films under a moving contactor [53]. The results reported in this work confirm that indeed the spatial variation in the wettability on the contactor can engender transitions from catastrophic to peeling to coalescence modes of debonding of the film from the contactor. Further, the study indicates that the contact instabilities guided by a moving patterned contactor have the capacity to

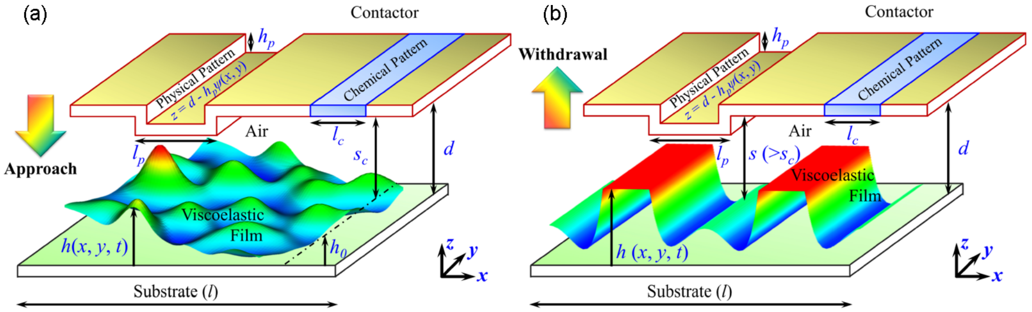

FIG. 1. Schematic representation of a thin viscoelastic film resting on a flat surface and confined by a contactor with topographic or chemical heterogeneities. The approach and the withdrawal of the contactor through the adhesion–debonding cycle are depicted in the images (a) and (b), respectively. During the *adhesion cycle*, the free film surface initiates deforming when the contactor attains a critical separation distance of s_c, with a finite velocity of v_c. Subsequently, surface patterns develop due to the contact instability and the contactor is pulled away from the contact vicinity during the *debonding cycle*. The notations, d, h_0, and s_0 ($=d - h_0$) denote the distance between the contactor and substrate, the base-state thickness of the film, and air gap, respectively. The variable local thickness of the film and the air gap is denoted by $h(x,y,t)$ and $s(x,y,t)$ ($=d - h(x,y,t)$). The height and the width of the topographic (chemical) patterns of the contactor are denoted by h_p and l_p (l_c). The patterned contactor is represented as $z = d - h_p\psi(x,y)$, where $\psi(x,y)$ is the shape function for physical heterogeneity.

improve the aspect ratio of the patterns by about fourfold than the same obtained by a homogeneous contactor. Example situations are shown where large area, higher aspect ratio nanostructures are decorated on the film surface employing the proposed methodology. In addition, the pathways to fabricate biomimetic prototypes, such as the large-area hierarchical patterns, have also been demonstrated.

The article is organized in the following manner. Section II contains the details of the governing equations and the boundary conditions required for the theoretical analysis. Section III summarizes the derivation of dimensionless nonlinear thin film evolution equations and numerical solution methodology of the same. The results are discussed and analyzed in detail in Sec. IV before we conclude by summarizing the key findings in Sec. V.

II. PROBLEM FORMULATION

Figure 1 schematically illustrates the adhesion-debonding cycle of the contact instabilities induced by the physically and chemically patterned contactors. Images (a) and (b) show the average (h_0) and variable thicknesses (h) of the films, separation distance (d) between the substrate (length l) and the contactor, the average (s_0) and variable (s) air gap between the film and contactor, width of chemical patch (l_c), and the width (l_p) and height (h_p) of the topographical patterns. The physically patterned contactor is described by the function, $z = d - h_p\ \psi(x,y)$, where $\psi(x,y)$ is a shape function. Image (a) shows the *adhesion cycle* in which the patterned contactor attains the critical separation distance, s_c, while approaching the film free surface with a velocity, v_c. The free surface of the viscoelastic film deforms due to the long-rage attractive van der Waals attraction with the contactor when it reaches the distance s_c from a very long separation distance. After the patterns are formed, the contactor is withdrawn during the *debonding cycle* from the film proximity at the same velocity, v_c, as schematically shown in the image (b).

A. Governing equations and boundary conditions

A three-dimensional Cartesian coordinate system (x, y, z) is used where the notations x and y represent the coordinates parallel to the substrate while the coordinate normal to the substrate surface is represented as z, and t represents time. We consider a thin film of zero-frequency linear viscoelastic soft solid with constant storage and loss moduli. The constitutive relation for such solids can be defined as [53,55–57],

$$\boldsymbol{\tau} = \mu(\nabla \mathbf{u} + \nabla \mathbf{u}^{\mathbf{T}}) + \eta(\nabla \dot{\mathbf{u}} + \nabla \dot{\mathbf{u}}^{\mathbf{T}}). \tag{1}$$

Here the symbols $\boldsymbol{\tau}$, $\mathbf{u}\{u,v,w\}$, μ, and η are stress tensor, displacement vector, storage modulus or elasticity, and loss modulus or viscosity of the film, respectively. The bracketed symbols denote the components of the displacement vector. The constitutive relation mimics the linear combination of a purely elastic spring and a purely viscous dashpot connected in parallel, which can capture the stress relaxation behaviors of the cross-linked polymers such as PDMS in the limit of small stress and small deformations under the influence of the destabilizing van der Waals force [53,55–57]. The constitutive equation is employed here to qualitatively uncover the morphological evolutions of the viscoelastic film in the limit of lubrication approximation. Inertial influences are neglected owing to the thinness of the viscoelastic films because, under the given conditions, the viscous forces are estimated to dominate over the inertial influences. Further, for the thin films undergoing contact instabilities, the body forces arising from the van der Waals forces are likely to be much stronger than the gravitational force.

It may be noted here that the nonlinear simulations shown in the present study are focused on the nonlinearities associated with the interfacial deformations in absence of the nonlinearities of the materials due to the large deformations under large stress. For this reason, the linear viscoelastic constitutive relation Eq. (1) is expected to serve the purpose [53,55–57]. This constitutive relation has previously been employed to explain the experimental results of polymer surface instabilities [54,58] or the findings related to the adhesion and debonding of polymers (such as PDMS [59]) with an approaching contactor [36,45]. In the present study, the results from the nonlinear simulations show a maximum strain of ∼1.5, while the maximum stress required to obtain such strain is ∼0.05 MPa. This is well within the limit of small-strain small-deformation systems as previously found in the experiments [7]. The stress-strain curve reported in this study matches with a number of previously reported experimental works on the soft-adhesives [5,8,60–69]. In fact, in the limit of lubrication approximation, the governing equations and boundary conditions involving the nonlinear neo-Hookean constitutive relation [8,70–76] lead to the same thin film equation, as shown in Sec. III.

The dynamics of such incompressible viscoelastic films can be described by the conservation of mass and momentum as

$$\nabla \cdot \mathbf{u} = 0, \tag{2}$$

$$-\nabla p + \nabla \cdot \boldsymbol{\tau} = 0, \tag{3}$$

where the pressure term, $p(=p_f - \pi)$ comprises of the pressure in the solid and the disjoining pressure p_f and π, respectively, and ∇ is the gradient operator. The viscoelastic film is assumed to be non-slipping on the impermeable substrate-film interface ($z = 0$),

$$\mathbf{u} = \dot{\mathbf{u}} = 0. \tag{4}$$

At the film-air interface ($z = h(x,y,t)$), we enforce the normal and tangential stress balances, and the kinematic condition as boundary conditions,

$$\mathbf{n} \cdot (-p_f \mathbf{I} + \boldsymbol{\tau}) \cdot \mathbf{n} = -\gamma\kappa, \tag{5}$$

$$\mathbf{n} \cdot \boldsymbol{\tau} \cdot \mathbf{t} = 0, \tag{6}$$

$$\dot{h} + \dot{\mathbf{u}} \cdot \nabla_s h = \dot{w}. \tag{7}$$

In these expressions, the overdots denote differentiation with respect to time, $\nabla_s(=(\mathbf{I} - \mathbf{nn}) \cdot \nabla)$ is surface gradient operator, and $\mathbf{I}$ is identity tensor. The unit outward normal ($\mathbf{n}$) and tangential ($\mathbf{t}$)

vectors are defined as, $\mathbf{n} = \{\nabla(z-h)/|\nabla(z-h)|\}$ and $\mathbf{n}\cdot\mathbf{t} = 0$, respectively. The symbol γ denotes the surface tension. The curvature of the free surface is defined as, $\kappa = \nabla_s \cdot \mathbf{n}$.

The disjoining pressure arising from the van der Waals interactions between the film, substrate, and contactor is defined as

$$\pi = -\frac{\partial \Delta G}{\partial h} = \frac{A_1}{6\pi(d-h_p\psi-h)^3} - \frac{A_2}{6\pi h^3} - \frac{3B}{(d-h_p\psi-h)^4}, \tag{8}$$

where ΔG represents the Gibbs free energy [49]. The effective Hamaker constants (A_i) are obtained from the binary Hamaker constants as $A_1 = A_{CF}$ and $A_2 = A_{FF} - A_{SF}$, where the subscripted notations S, C, and F represent the substrate, contactor, and film, respectively. The free surface of the film is deforming because of the intermolecular interaction between the contactor and the film through the air gap of $(d-h_p\psi-h)$, when the effective Hamaker constant, $A_1 > 0$ [49,53]. We consider the viscoelastic film to be wetting the substrate leading to the Hamaker constant, A_2, to be less than zero. The shape function ψ takes into account the influence of the physical heterogeneity on the contactor. The contact-line-singularity at the film-contactor interface during the attachment of the film is evaded by the inclusion of the short-range Born repulsion (B) term in the expression of the disjoining pressure. The expression for B is obtained from the condition $\pi((d-h_p\psi-h)\to l_0) = 0$, as

$$B = \frac{l_0^4}{18\pi}\left(\frac{A_1}{l_0^3} + \frac{A_2}{(d-h_p\psi-l_0)^3}\right), \tag{9}$$

in which, l_0 represents the equilibrium cutoff thickness [49,53]. The adhesive energy per unit area during contact is obtained by the minimization of free energy at the equilibrium distance (l_0) as [53]

$$\Delta G_0 = -\frac{1}{36\pi}\left(\frac{A_1}{l_0^2} + \frac{A_2(3d-3h_p\psi-l_0)}{(d-h_p\psi-l_0)^3}\right). \tag{10}$$

B. Derivation of thin film equations

The spatiotemporal evolution of the deforming free surface of the thin viscoelastic film is theoretically modeled in the long-wave limit [53–57]. Thus, the simplified continuity and momentum equations are as follows:

$$u_x + v_y + w_z = 0, \tag{11}$$

$$\mu u_{zz} + \eta \dot{u}_{zz} = p_x, \tag{12}$$

$$\mu v_{zz} + \eta \dot{v}_{zz} = p_y, \tag{13}$$

$$p_z = 0. \tag{14}$$

The subscripts x, y, and z represent partial differentiation. Parabolic profile for u and v are assumed and incorporated in the above Eqs. (11)–(14) as

$$u = c_1(x,y,t)z^2 + c_2(x,y,t)z + c_3(x,y,t), \tag{15}$$

$$v = c_4(x,y,t)z^2 + c_5(x,y,t)z + c_6(x,y,t), \tag{16}$$

where the variables (c_2 and c_5) and (c_1 and c_4) denote the shear stresses and divergence of the shear stresses, respectively [53,57], while c_3 and c_6 are constants. The constants for the solutions are evaluated with the help of no-slip and impermeability boundary conditions at the film-substrate interface ($z = 0$),

$$u = v = 0, \tag{17}$$

$$w = 0. \tag{18}$$

The balances of normal and tangential stresses are enforced at the film-air interface ($z = h(x,y,t)$) [53,55–57] as boundary conditions,

$$p + \pi + \gamma(h_{xx} + h_{yy}) = 0, \tag{19}$$

$$\mu u_z + \eta \dot{u}_z = 0, \quad \mu v_z + \eta \dot{v}_z = 0. \tag{20}$$

The z-directional displacement (w) is obtained from the x- and y-directional displacements and the continuity equation. The expressions for the displacements are replaced in the kinematic condition,

$$\dot{h} + \dot{u} h_x + \dot{v} h_y = \dot{w}, \tag{21}$$

to obtain the following set of nonlinear partial differential equations (PDEs) for the evolving free surface of the viscoelastic film undergoing contact instability,

$$\dot{h} - \frac{1}{\eta}\nabla \cdot \left[\frac{h^3}{3}\nabla p + \frac{\mu h^3}{3}(c_1\mathbf{e_x} + c_4\mathbf{e_y}) + \frac{\mu h^2}{2}(c_2\mathbf{e_x} + c_5\mathbf{e_y})\right] = 0, \tag{22}$$

$$\eta \dot{c}_1 - (0.5 p_x - \mu c_1) = 0, \quad \eta \dot{c}_4 - (0.5 p_y - \mu c_4) = 0, \tag{23}$$

$$\eta \dot{c}_2 + (h p_x + \mu c_2) = 0, \quad \eta \dot{c}_5 + (h p_y + \mu c_5) = 0, \tag{24}$$

where

$$p = -\frac{1}{6\pi}\left(\frac{A_1}{(d - h_p\psi - h)^3} - \frac{A_2}{h^3} - \frac{l_0^4}{(d - h_p\psi - h)^4}\left(\frac{A_1}{l_0^3} - \frac{A_2}{(d - h_p\psi - l_0)^3}\right)\right)$$
$$- \gamma(h_{xx} + h_{yy}). \tag{25}$$

The detailed steps of the derivation [53] are given in Appendix A. It may be noted here that, in the limit of lubrication approximation, the governing equations and boundary conditions involving the nonlinear neo-Hookean constitutive relation [8,70–76] also lead to the same set of thin film equations, as shown in Eqs. (21)–(25). A brief summary of the steps to derive such equations involving the neo-Hookean model is provided in Appendix B. The effective pressure (p) is obtained from the normal stress balance. The symbols ($\mathbf{e_x}$, $\mathbf{e_y}$) represent the unit vectors of x- and y-directions, respectively. The movement of the contactor during the adhesion-debonding cycle is incorporated in the set of evolution Eqs. (22)–(24) as [53]

$$d = d_0 \mp v_c t, \tag{26}$$

where negative and positive signs represent the approach and withdrawal of the contactor, respectively. Here, d_0 is the initial separation distance between the contactor and the substrate. The expressions for the local normal stresses (σ_n) on the free surface, the pull-off force (F_d) per unit area, and the work per unit area (W) required to pull the contactor from s_c to s_0 (any separation distance) can be evaluated from the following expressions [52,53],

$$\sigma_n(x,y,h) = -p, \tag{27}$$

$$F_d = (1/l^2)\int_0^l \int_0^l p\, dx\, dy, \tag{28}$$

$$W = \int_{s_c}^{s_0} F_d\, dz. \tag{29}$$

The total work done per unit area during the debonding cycle is calculated by changing the upper limit of the integration of Eq. (29) from any separation distance (s_0) to the snap-off distance (s_p), where the film detaches from the contactor.

C. Wettability gradients on the heterogeneous surfaces

The disjoining pressure, $\pi(s,x,y)$, for a configuration where a thin viscoelastic film is deforming due to the intersurface adhesive interaction with a predecorated contactor having physical or chemical patterns can be represented as [47]

$$d\pi = \left(\frac{\partial \pi}{\partial s}\right)\bigg|_{x,y} ds + \left(\frac{\partial \pi}{\partial x}\right)\bigg|_{y,s} dx + \left(\frac{\partial \pi}{\partial y}\right)\bigg|_{x,s} dy. \tag{30}$$

The gradient of the disjoining pressure has two significantly different mechanisms in Eq. (30). The first term signifies the variation in the pressure due to the separation distance between the film and the contactor, which can initiate the contact instability even when the surface is homogeneous in nature. Additionally, the second and the third term arise because of the spatial variations in the wettability with the variation in the (i) distance between the film and the contactor when physical heterogeneities are present, and (ii) the Hamaker constant of the contactor when the chemical heterogeneities are present. Thus, the second and the third terms in Eq. (30) helps in directing the free surface patterns when approached by a contactor having pre-decorated periodic physical or chemical patterns. For example, for a periodically patterned physically heterogeneous surface the air gap is expected to be smaller in the protruded regions where the free surface may deform faster to develop a pattern-directed contact instability. Similarly, a contactor with the periodic chemical patches can cause a faster deformation of the free surface selectively in the zones of higher wettability (larger magnitude of Hamaker constant, A_{1h}) owing to the presence of the stronger van der Waals interaction. In that situation, the adhesive energy per unit area (ΔG_0) and the expression for pressure (p) at the zone having Hamaker constant, A_{1h}, changes to

$$\Delta G_0 = -\frac{1}{36\pi}\left(\frac{A_{1h}}{l_0^2} + \frac{A_2(3d - 3h_p\psi - l_0)}{(d - h_p\psi - l_0)^3}\right), \tag{31}$$

$$p = -\frac{1}{6\pi}\left(\frac{A_{1h}}{(d - h_p\psi - h)^3} - \frac{A_2}{h^3} - \frac{l_0^4}{(d - h_p\psi - h)^4}\left(\frac{A_{1h}}{l_0^3} - \frac{A_2}{(d - h_p\psi - l_0)^3}\right)\right) - \gamma(h_{xx} + h_{yy}), \tag{32}$$

which alter σ_n, F_d, and W, according to the Eqs. (27)–(29).

III. DIMENSIONLESS FORMS

A series of nonlinear simulations have been performed to investigate the spatiotemporal evolution of a thin viscoelastic film confined by a patterned contactor. For this purpose, the nonlinear PDEs in Eqs. (22)–(24) are made dimensionless employing the following scales: length $\sim h_0$, time $\sim \eta/\mu$, velocity $\sim \mu h_0/\eta$, and pressure $\sim \mu$. These scaling parameters lead to the following set of nondimensional parameters: $(H,H_p) = (h,h_p)/h_0$, $(D,D_0) = (d,d_0)/h_0$, $L = l_0/h_0$, $V = \eta v_c/\mu h_0$, $(S,S_0,S_c,S_p,S_e) = (s,s_0,s_c,s_p,s_e)/h_0$, $(L_p,L_c) = (l_p,l_c)/h_0$, $P = p/\mu$, $A_r = A_2/A_1$, $\bar{A} = A_1/6\pi\mu h_0^3$, $\bar{\mu} = \mu h_0/\gamma$, $X = x/h_0$, $(C_1,C_4) = (c_1,c_4)h_0$, $(C_2,C_5) = (c_2,c_5)$, $\sum_n = \sigma_n/\mu$, and $T = \mu t/\eta$, where S_e is the dimensionless effective separation distance. The set of subsequent nondimensional coupled nonlinear PDEs for the evolving free surface is [53]

$$\frac{\partial H}{\partial T} - \frac{1}{3}\nabla\cdot\left(H^3\nabla P + H^3(C_1\mathbf{e_x} + C_4\mathbf{e_y}) + \frac{3}{2}H^2(C_2\mathbf{e_x} + C_5\mathbf{e_y})\right) = 0, \tag{33}$$

$$\frac{\partial C_1}{\partial T} - \left(\frac{1}{2}\left(\frac{\partial P}{\partial X}\right) - C_1\right) = 0, \quad \frac{\partial C_4}{\partial T} - \left(\frac{1}{2}\left(\frac{\partial P}{\partial Y}\right) - C_4\right) = 0, \tag{34}$$

$$\frac{\partial C_2}{\partial T} + \left(H\left(\frac{\partial P}{\partial X}\right) + C_2\right) = 0, \quad \frac{\partial C_5}{\partial T} + \left(H\left(\frac{\partial P}{\partial Y}\right) + C_5\right) = 0, \tag{35}$$

where

$$P = -\bar{A}\left(\frac{1}{(D - H_p\psi - H)^3} - \frac{A_r}{H^3} - \frac{L^4}{(D - H_p\psi - H)^4}\left(\frac{1}{L^3} - \frac{A_r}{\left(D - H_p\psi - L\right)^3}\right)\right) - \frac{1}{\bar{\mu}}\left(\frac{\partial^2 H}{\partial X^2} + \frac{\partial^2 H}{\partial Y^2}\right), \tag{36}$$

$$D = D_0 \mp VT. \tag{37}$$

Dimensionless normal shear stress is expressed as, $\sum_n = -P$. The nondimensional adhesive energy per unit area is expressed as

$$\Delta G_{\mathrm{ND}} = \frac{\Delta G_0 h_0^2}{A_1} = -\frac{1}{36\pi}\left(\frac{1}{L^2} + \frac{A_r(3D - 3H_p\psi - L)}{(D - H_p\psi - L)^3}\right). \tag{38}$$

First, the set of nonlinear fourth-order PDEs Eqs. (30)–(32) are discretized in space using central difference with half-node interpolation. Then the resultant set of stiff coupled ordinary differential equations (ODEs) for each discretized point is solved in time using Gear's algorithm from the subroutine D02NCF of the NAG library. Random perturbation with volume conservation at the film-air free interface, $H(X,Y,T)$, has been employed as an initial condition for the numerical simulations. The spatial periodic boundary conditions (PBCs) have been enforced to obtain results consistent with a large area. The domain sizes for the computations are chosen to be the multiples of the nondimensional dominant wavelength of the instability, Λ_m, which is evaluated from the linear stability analysis of Eqs. (33)–(35) for a homogeneous contactor ($\psi = 0$) [53]. The number of grid points is varied to test the grid independence of the solutions before the results are reported for this work. The physical heterogeneity on the contactor has been incorporated by changing air gap thickness locally, whereas the chemical heterogeneity is introduced by locally tuning the Hamaker constants of the contactor.

IV. RESULTS & DISCUSSION

In this section, we analyze the spatiotemporal evolutions of a deforming thin viscoelastic film during the adhesion-debonding with a patterned contactor. In comparison to the previous works, the uniqueness of these simulations is the use of a finite velocity to the patterned contactor while it approaches the film as well as when pulled away from the film-proximity. In the process, we have shown the recipes to form some interesting large-area micro- or nanopatterns on the thin viscoelastic films. It may be noted here that unless mentioned otherwise, we carry out all the simulations in the following manner: (i) during the *adhesion cycle*, the patterned contactor is bought from a large separation distance ($S \gg S_c$) to an effective separation distance, S_e ($\leqslant S_c$), at a constant velocity V; (ii) the film remains stable until the patterned contactor crosses S_c and at S_e the film surface develops the patterns induced by the inter-surface adhesive interaction; (iii) thereafter, we allow the contact instabilities to mature as the free surface of the viscoelastic film progressively comes in contact with the patterned contactor; (iv) following this, in the *debonding cycle*, we perform the pull-off of the patterned contactor at a velocity, V. It may be noted that the darker shades in the top and isometric views shown indicate larger magnitude in the "z" direction.

Figure 2 shows the surface morphologies of the viscoelastic films [columns (b)–(e) in Fig. 2] during the adhesion and debonding of a topographically patterned contactor with periodic ridges and valleys. The images in column (a) in Fig. 2 show the ridges and valleys predecorated on the contactor having a periodicity of Λ. In this figure, the different pathways of debonding, such as peeling (rows I and II), catastrophic (rows III and IV), and coalescence (rows V and VI) modes, have been engendered by varying the compliance ratio ($C_R = E_C/V_C$) of the films. Here, $E_C = \Delta G_0 h_0/\mu l_0^2$ and $V_C = \Delta G_0/\eta v_c$ denote the elastic and viscous compliances of the film. The topographically patterned contactor ensures that the destabilizing van der Waals force is stronger near the protrusions.

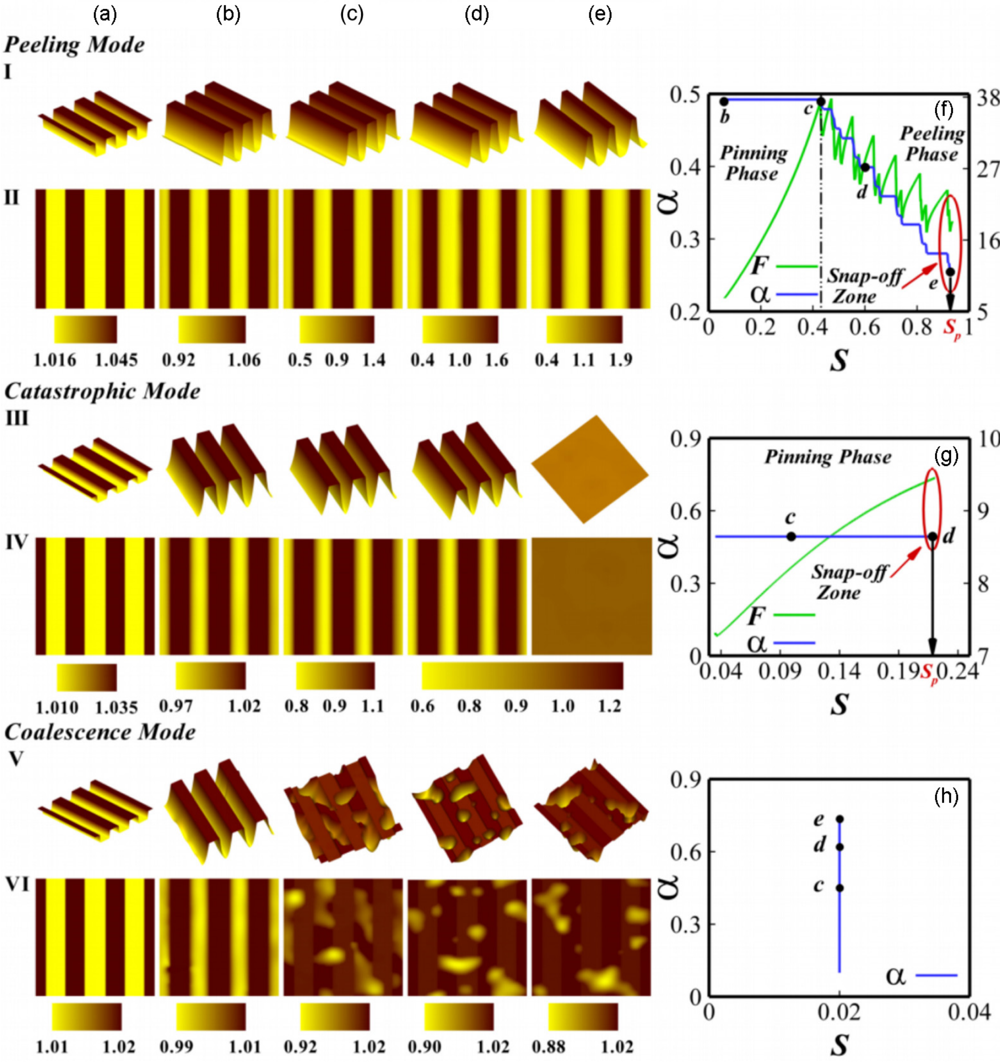

FIG. 2. The nonlinear space-time evolutions of the viscoelastic film undergoing peeling, catastrophic, and coalescence modes of debonding in the presence of a periodically striped pattern contactor ($L_p = \Lambda/2$) in a $3\Lambda \times 3\Lambda$ domain when the compliance ratio (C_R) of the film is varied. Column (a) depicts the contactor geometries while columns (b)–(e) show the morphological evolution of the free film-air interface at time $T = 0.2$, 1.4, 2.5, and 3.6 for rows (I) and (II), $T = 0.002$, 0.012, 0.2, and 0.3 for rows (III) and (IV), and $T = 0.4, 4.4, 22.7$, and 40.7 for rows (V) and (VI). Rows (I), (III), and (V) [(II), (IV), and (VI)] show the isometric [top] views of the images. Plots (f)–(h) show the variations in the fractional contact area (α) and average pull-off force (F) with the separation distance (S) of the systems shown in the same row. The compliance ratio, for peeling mode, $C_R = 2.7 \times 10^4$ ($\mu = 10^3$ Pa, $s_e = 45$ nm, and $v_c = 250\ \mu$m/s); for catastrophic mode, $C_R = 1.1 \times 10^3$ ($\mu = 10^2$ Pa, $s_e = 40$ nm, and $v_c = 1\ \mu$m/s); for coalescence mode, $C_R = 1.0 \times 10^{-4}$ ($\mu = 10^6$ Pa, $s_e = 20$ nm, and $v_c = 1$ nm/s). The amplitudes of the physical heterogeneities (H_p) employed for the simulations are $\sim 0.03\ H$ [rows (I) and (II)], $\sim 0.025\ H$ [rows (III) and (IV)], and $\sim 0.01\ H$ [rows (V) and (VI)], where H is the dimensionless film thickness. Other typical parameters used for the simulations are enlisted in Table I.

TABLE I. Parametric values used in the simulations.

Variables	Values
ΔG_0 (mJ m^{-2})	0.5
η (Pa s)	1.0
h_0 (μm)	1.0
γ (mN m^{-1})	30.0
μ (Pa)	1000
s_e (nm)	40.0
v_c (μm s^{-1})	1000
l_0 (nm)	3.0
Λ (μm)	8.7

Thus, in short time, the free surface of the viscoelastic film develops stripe patterns under the protrusions following the periodicity of the contactor patterns, as shown in the images of column (b) in Fig. 2. Thereafter, the patterned contactor is pulled away from the contact proximity with a velocity of V, as shown in the images (c)–(e) in Fig. 2. To perform complete debonding, the contactor is taken away from the film-proximity until the film is completely separated from the contactor at the snap-off distance (S_p). Previous works reveal that the compliance ratio (C_R) is one of the deciding factors for the changeover of the debonding modes in which the peeling (coalescence) mode is expected when C_R is high (low), whereas at intermediate C_R the catastrophic mode is observed [53]. In the similar lines, images (b) and (c) of rows (I) and (II) in Fig. 2 show that during the debonding, at higher values of C_R ($E_c = 5.5 \times 10^4$, $V_c = 2.0$) the stripes initially get elongated at a constant area of contact leading to a "pinning" phase. Following this, a "peeling" phase is observed where a progressive reduction in the area of contact takes place, as shown in the images (c)–(e) of rows (I) and (II) in Fig. 2. The film peels out completely from the patterned contactor at S_p.

Plot (f) in Fig. 2 shows the typical nonmonotonic variation in the fractional contact area (α) with the separation distance (S) for the peeling mode where α progressively reduces during the stepwise peeling of the film from the contactor. However, α remains constant during the intermediate pinning phases while stepwise peeling occurs. Plot (f) in Fig. 2 also shows that the average pull-off force (F) required per unit area during the pull-off phase increases to a maximum value at the end of the pinning phase before the peeling of the film starts. The plot uncovers that whenever the stress levels at the edges of the columns increase beyond a threshold value, the film relaxes the stress by decreasing contact area from the sides of the columns to engender the peeling mode. For this reason, we observe a series of progressive increase and then sharp fall in the magnitude of F during the stepwise peeling of the film from the striped contactor, which signifies the requirement of maximum F before a part of the film snaps back from the patterned contactor. Incidentally, each of this stepwise decrease in the area of contact actually signifies a catastrophic adhesion failure for stress relaxation. The results also corroborate that the pre-decorated protrusions on the contactor help in increasing the snap-off (S_p) distance significantly as compared to a similar system with a homogeneous contactor. For example, the contact instabilities of viscoelastic films of 1 µm thick can develop surface patterns of height ~1 μm ($S_p = 0.9$) under a patterned contactor as compared to ~250 nm ($S_p = 0.025$) under a homogenous contactor [53]. In comparison, the use of patterned contactor can lead to an at least fourfold increase in the aspect ratio of the micropatterns fabricated on the surface of a viscoelastic film. The aspect ratio ($A_r = H_s/0.5\Lambda$, where H_s is the height of stripe patterns) of the stripes shown in the image (e) of rows (I) and (II) is evaluated to be ≈0.35, which is comparable ($A_r \approx 0.28$) to a recent experimental study [45].

The images (b)–(e) of rows (III) and (IV) in Fig. 2 show the catastrophic mode of debonding where the stripes elongate without peeling [images (b)–(d) in Fig. 2] until sudden snap-off from the contactor [image (e) in Fig. 2] takes place. The plot (g) in Fig. 2 shows that for this mode the fractional area (α) of contact remains constant and the pull-off force per unit area increases monotonically until the contact between the film and the contactor is abruptly reduced to zero. This mode prevails when C_R is in the intermediate regime, for example, when the film has more elastic (E_C) as well as viscous compliance (V_C). At rather lower values of low C_R when the viscous compliance dominates over the elastic one, the coalescence mode of debonding of the viscoelastic films is observed, as shown in the rows (V) and (IV). The images (b)–(e) in Fig. 2 show the stripes developed on the free surface of the viscoelastic film rapidly coalesce while the debonding takes place. The coalescence is signified merging of the film surface between the stripes, which is also associated with the formation of the random zones of depressions or holes at different places. Plot (h) in Fig. 2 shows an abrupt increase in α in this mode due to the rapid coalescence of patterns makes the debonding process rather difficult.

Concisely, results obtained in Fig. 2 show that, although the debonding pathways remain similar for both the physically homogeneous and heterogeneous contactors, the snap-off distance can be significantly improved by the use of a patterned contactor. This opens up the possibility of developing patterns with higher aspect ratios when the ECL is performed employing a physically heterogeneous contactor.

Previously, we mentioned that the compliance ratio (C_R) of a thin viscoelastic film can cause the changeover of debonding modes from catastrophic to peeling to coalescence [53]. In Figs. 3 and 4,

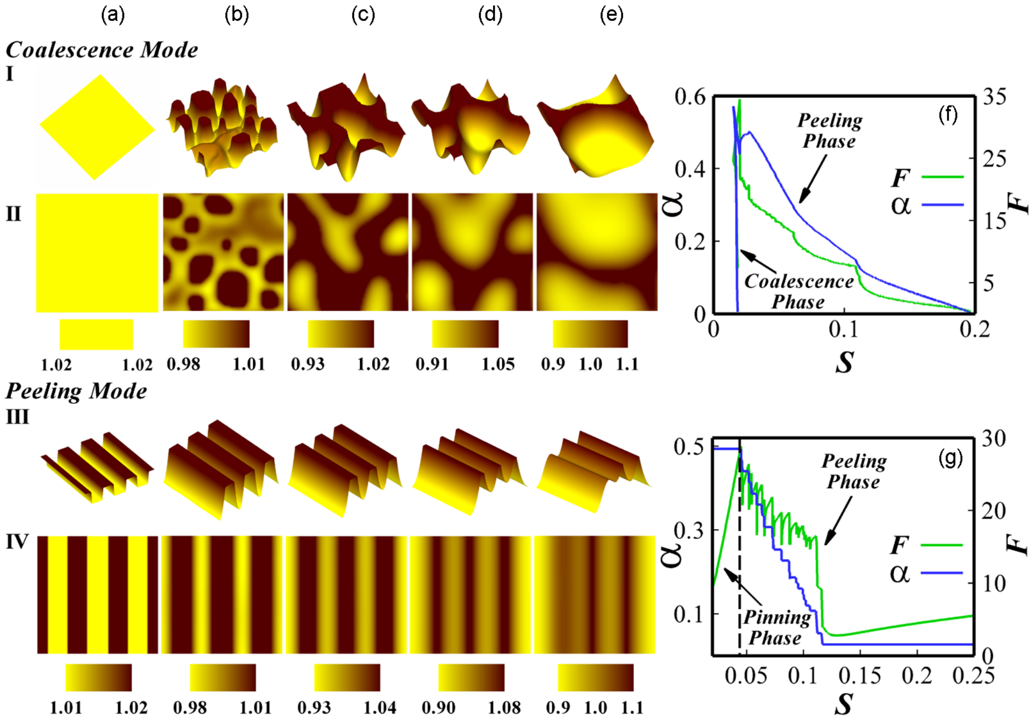

FIG. 3. The nonlinear space-time evolutions of the viscoelastic film showing the transition from coalescence to peeling mode with the use of striped pattern contactor ($L_p = \Lambda/2$, $H_p = 0.01\,H$) instead of a homogeneous contactor in a $3\Lambda \times 3\Lambda$ domain. Column (a) depicts the contactor geometries while columns (b)–(e) show the morphological evolution of the thin film free surface at time $T = 0.002$, 0.014, 0.04, and 0.09 for rows (I) and (II) and $T = 0.003$, 0.04, 0.08, and 0.09 for rows (III) and (IV). Rows (I) and (III) [(II) and (IV), respectively] show the isometric [top] views of the images. Plots (f) and (g) show the variations in α and F with S of the systems shown in the same row. Compliance ratio for both the modes mode is $C_R = 1.1 \times 10^5$ ($s_e = 20\,\text{nm}$). Other dimensional parameters are listed in Table I.

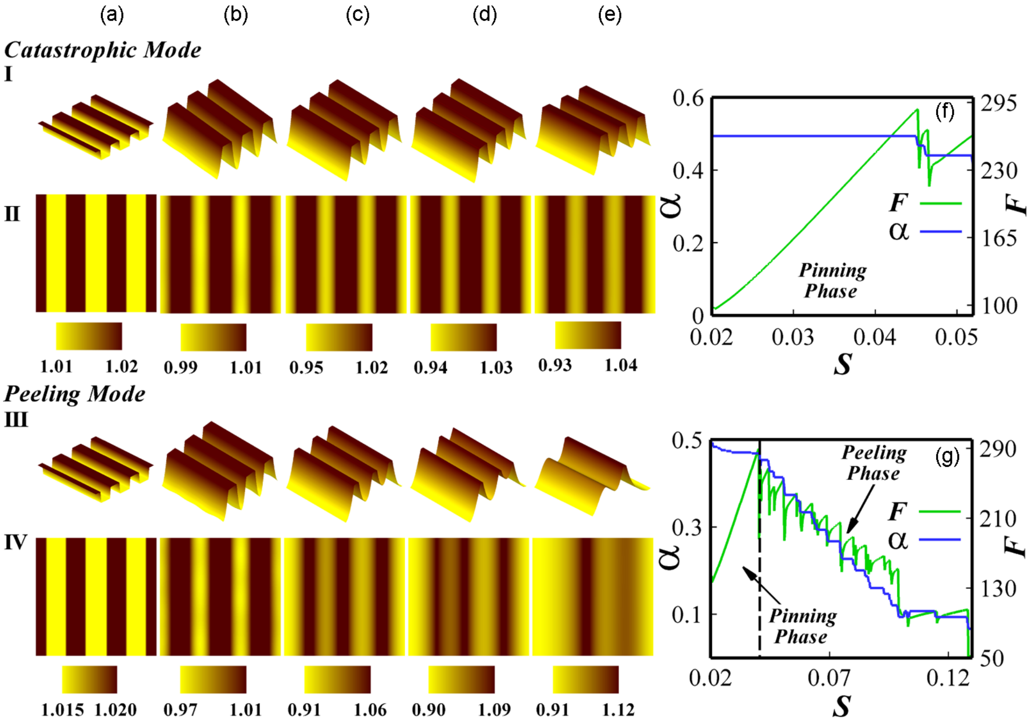

FIG. 4. The nonlinear space-time evolutions of the viscoelastic film showing the transition from the catastrophic to peeling mode with the reduction in height (H_p) of the stripe patterns on the contactor $(L_p = \Lambda/2)$ from 0.01 H to 0.005 H, respectively, in a $3\Lambda \times 3\Lambda$ domain. Column (a) depicts the contactor geometries while columns (b)–(e) show the morphological evolution of the thin film-air interface at time $T = 0.0002$, 0.002, 0.003, and 0.004 for rows (I) and (II) and $T = 0.0002$, 0.006, 0.008, and 0.01 for rows (III) and (IV). Rows (I) and (III) [(II) and (IV)] show the isometric [top] views of the images. Plots (f) and (g) show the variations in α and F with S of the systems shown in the same rows. Compliance ratio for both the modes mode is $C_R = 1.1 \times 10^6$ ($s_e = 20\,\text{nm}$, $\mu = 10^2\,\text{Pa}$). Typical dimensional parameters are listed in Table I.

we show that this is even possible when the amplitude of the physical heterogeneity of the contactor is changed at a constant C_R.

Images (b)–(e) of rows (I) and (II) of Fig. 3 show the coalescence mode of contact instability when a homogeneous contactor is deployed [images (a) of Fig. 3], which is converted into a peeling mode [rows (III) and (IV) of Fig. 3] when the contactor possesses periodic ridges and valleys [image (a) of Fig. 3]. In this situation, in short time, the protrusions on the contactor ensure the formation of stripe patterns on the film surface during the adhesion cycle before any coalescence is initiated. Figure 3 shows a typical example where a transition of modes from coalescence to peeling mode takes place due to the presence of physical heterogeneity on the contactor surface. Plots (f) and (g) of Fig. 3 show the characteristic variations in α and F with S, which also confirm the transition from coalescence to the peeling mode with the introduction of the physical heterogeneity. Plot (g) of Fig. 3 also depicts that contact area, α, remains constant for a long time before the snap-off takes place. This because a high viscous compliance enables the film to undergo rapid coalescence under a single stripe during the adhesion cycle before the patterned contactor is pulled away.

Figure 4 shows an example where a change over from catastrophic to peeling mode takes place with the use of patterned contactor at a constant C_R. The rows (I) and (II) show a catastrophic mode of debonding under a physically heterogeneous contactor while rows (III) and (IV) show the peeling mode of debonding when the amplitude of the protrusions on the contactor is reduced.

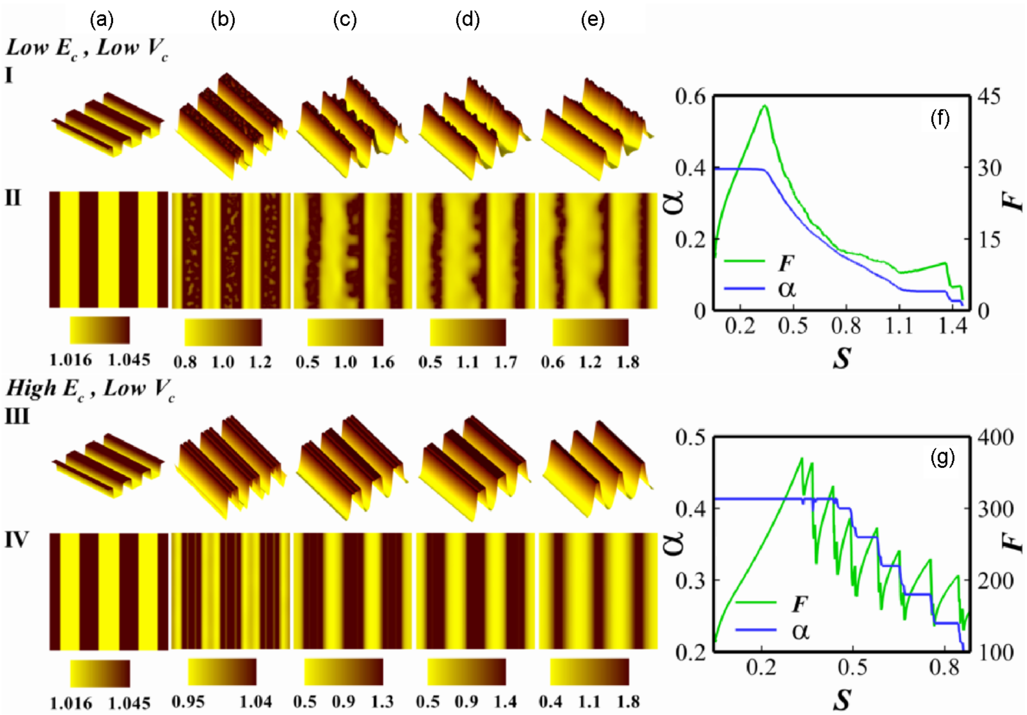

FIG. 5. Spatiotemporal evolutions of viscoelastic films with the variations in the elastic and viscous compliances (E_c and V_c) in a $3\Lambda \times 3\Lambda$ domain. Column (a) depicts the contactor geometries and columns (b)–(e) show the morphological evolution of the free surface of the thin film at time $T = 0.2$, 0.6, 0.8, and 1.1 for rows (I) and (II) and $T = 0.004$, 0.03, 0.04, and 0.08 for rows (III) and (IV). Rows (I) and (III) show the isometric profiles and rows (II) and (IV) show the top views. Plots (f) and (g) show the variations in α and F with S of the systems shown in the same row. The width of the stripe patterns on the patterned contactor for rows (I)–(IV) are $L_p = \Lambda/2$ and the height of the patterns for rows (I)–(IV) are $H_p = 0.03\,H$. The elasticity of the film used for rows (III) and (IV) is $\mu = 10^2$ Pa. The other parameters used are listed in Table I.

Images (b)–(d) of rows (I) and (II) of Fig. 4 collectively with the plot (f) of Fig. 4 suggest the catastrophic mode of debonding happens when the amplitude of the protrusions of the contactor is larger [image (a) of Fig. 4]. In contrast, the images (b)–(e) of rows (III) and (IV) of Fig. 4 and the plot (g) of Fig. 4 show the changeover to the peeling mode when the amplitude of the protrusions is reduced [image (a) of Fig. 4]. In this case, the reduction in pattern height reduces the adhesive energy near the protrusions. The results shown in Figs. 3 and 4 open up the possibility of developing the peeling mode of debonding for a viscoelastic film for a wider range of C_R when a physically patterned contactor is used in place of a homogeneous one. This is important from the context of developing surface patterns with higher aspect ratio because, previously, it is shown that among all the debonding pathways the peeling mode has the capacity to form the ordered patterns with largest aspect ratio on the surface of a thin viscoelastic film.

Figure 5 shows the influence of elastic (E_C) and viscous (V_C) compliances on the free surface morphologies of the viscoelastic films in the peeling mode. Previously, the rows (I) and (II) in Fig. 2 show an example where the peeling mode of debonding led to a snap-off distance $S_p \sim 1$. A previous work [53] has reported that the decrease in V_C (higher C_R) can improve S_p further because of the increase in the withdrawal velocity (V), which can be one of the ways to develop patterns with higher aspect ratios than the same obtained in Fig. 2. The images in the rows (I) and (II) of Fig. 5 show the results for the same system as shown in Fig. 2 with a lower V_C (=0.5) because of a higher pull-off velocity ($v_c = 1000\,\mu\text{m/s}$) of the contactor during debonding keeping E_c fixed

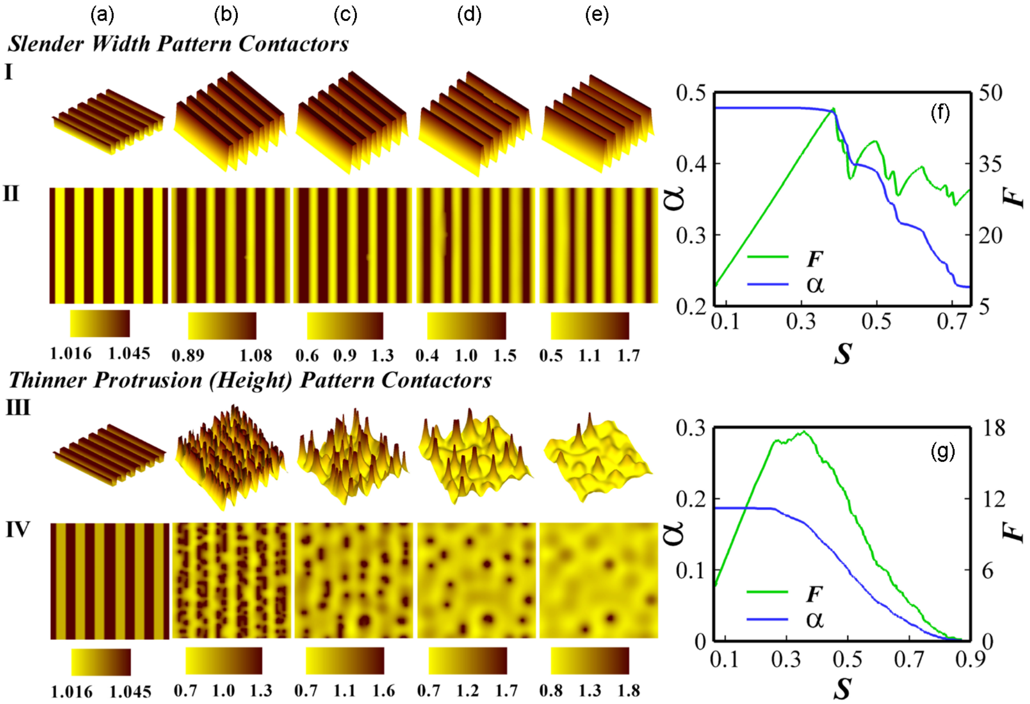

FIG. 6. Spatiotemporal evolutions of viscoelastic films with the variations in the width (L_p) and the amplitude (H_p) of the stripe patterns on the contactor in a $3\Lambda \times 3\Lambda$ domain. Column (a) depicts the contactor geometries and columns (b)–(e) show the morphological evolution of the free surface of the thin film at time $T = 0.07$, 0.3, 0.5, and 0.7 for rows (I) and (II) and $T = 0.3$, 0.6, 0.7, and 0.8 for rows (III) and (IV). Rows (I) and (III) show the isometric profiles and rows (II) and (IV) show the top views. Plots (f) and (g) show the variations in α and F with S of the systems shown in the same row. The width of the stripe patterns on the patterned contactor for rows (I)–(IV) are $L_p = \Lambda/4$ and the height of the patterns for rows (I) and (II) [(III) and (IV)] are $H_p = 0.03\,H$ [$H_p = 0.01\,H$]. The other parameters used are listed in Table I.

($E_c = 5.5 \times 10^4$). Plot (f) of Fig. 5 confirms that indeed the S_p of the ridges can be improved up to $S_p \sim 1.4$ by this method, which is also reflected in the images (b)–(e) of Fig. 5. In fact, near the snap-off stage of debonding, the ridges on the left side of the viscoelastic film undergoes a Plateau-Rayleigh instability to transform into discrete columnar patterns, as shown by the images (c)–(e) of Fig. 5. In this scenario, increasing the elastic compliance ($E_C = 5.5 \times 10^5$) by decreasing the elasticity of the film (μ) can arrest the Plateau-Rayleigh instability before snap off to restore the stripe patterns, as shown in the plots (b)–(e) of rows (III) and (IV) of Fig. 5. However, increase in E_C also causes a reduction in the snap-off distance ($S_p \sim 0.8$) than the same obtained for the system shown in Fig. 2. The results shown in Fig. 5 highlight the necessity to find the optimal condition by tuning the compliance ratio (C_R) and speed of the contactor (V) to obtain higher aspect ratio features with large area ordering using ECL.

Figure 6 shows the ordering of the microstructures when the height (H_p), width (L_p), and periodicity of the stripe patterns on the contactor are varied. The figure suggests that a smaller periodicity of the stripes can be employed to reduce the spacing of the ridges formed on the surface of the film. For example, rows (I) and (II) of Fig. 6 show that when the stripe periodicity is $\Lambda/2$ ($L_p = \Lambda/4$) on the contactor, periodic ridges with the same periodicity appear on the film surface. The patterns on the film surface last until the snap-off takes place at, $S_p \sim 0.75$, as shown in plot (f) of Fig. 6. In comparison, keeping the other parameters same, when the height of the stripes of the contactor is reduced ($H_p = 0.01\,H$), again the ridges on the film shows Plateau-Rayleigh instability before snap-off to form columnar structures, as shown by the images in rows (III) and (IV) of Fig. 6. In this condition, the order of the patterns developed on the film surface disappears during debonding phase, as shown by the images (c)–(e) of Fig. 6. In this case, a significantly large film-contactor separation distance and a smaller amplitude of the physical patterns on the contactor brings back the signature of the contact instabilities of a viscoelastic film under a homogeneous contactor. Briefly, Fig. 6 suggests that height (H_p), width (L_p), and periodicity of the stripe patterns predecorated on the contactor can influence the aspect ratio and order of the patterns developed during the pattern-directed contact instabilities of thin viscoelastic films.

A chemically heterogeneous contactor can also show a transition from coalescence to peeling to catastrophic modes at a constant C_R, as shown in Fig. 7. Rows (I) and (II) of Fig. 7 show a coalescence mode of debonding of the thin film in the presence of a contactor having a homogeneous adhesive energy (ΔG_0), as shown in image (a) of Fig. 7. Images (b) and (c) of Fig. 7 in these rows show the coalescence of the irregular shaped thin film columns while images (d) and (e) of Fig. 7 show the growth of the cavities with the elongation of the coalesced microstructures. The abrupt initial increase in α and F in the plot (f) of Fig. 7 confirm that indeed coalescence of the microstructures happen before peeling starts to form big cavities to initiate the cohesive failure of the film. We can observe the peeling [rows (III) and (IV) of Fig. 7] and catastrophic [rows (V) and (VI) of Fig. 7] modes of debonding when a chemically heterogeneous contactor is employed with chemical patches of higher adhesive energy, $\Delta G_0^h > \Delta G_0^l$, on the darker zones and smaller one (ΔG_0^l) in the lighter zones. The typical checkerboard pattern of the chemically heterogeneous contactor is shown in image (a) of the rows (III)–(VI) of Fig. 7. Again, the transition of the debonding modes is found to have a similar origin, as previously observed for the physically heterogeneous contactor. The darker chemical patches with larger adhesive force have stimulated the formation of box-patterns on the surface of the viscoelastic film before any coalescence is initiated, which results in the transition from coalescence to peeling mode of debonding.

In general, when the contrast of adhesive energy ($\Delta G_R = \Delta G_0^h/\Delta G_0^l$) across the chemically heterogeneous contactor is moderately high ($\Delta G_R \sim 10$), the peeling mode is observed. However, the figure also suggests that at a high $\Delta G_R \sim 100$ the catastrophic mode prevails. Remarkably enough, the snap-off distance improves by approximately threefold than the same obtained in the peeling mode for the topographically patterned contactor. Concisely, Fig. 7 reveals some simple recipes to develop higher aspect ratio structures with large-area ordering on a thin viscoelastic film undergoing contact instability using a chemically heterogeneous contactor.

Figure 8 shows a few examples to develop large-area ordered patterns with higher aspect ratio exploiting the pattern-directed contact instabilities of the thin viscoelastic films. The procedures to calculate the aspect ratio (A_r) and the taper ratio (T_r) of the structures is shown in plot (i) of Fig. 8. The magnitude of the taper ratio (T_r) provides the information on the shape and geometry of the structures. For example, $T_r = 1$ signifies a cylindrical columnar structure of uniform radius whereas the reduction in the value of T_r indicates conical frustum shapes with increased angle of inclination. Images (a) and (b) in case I of Fig. 8 show that a viscoelastic film deforming under homogeneous contactor forms columns with an average aspect ratio of $A_r \approx 0.18$. Case I of Fig. 8 shows that a taper ratio around $T_r \approx 0.49$ is obtained for the microstructures formed using a homogeneous contactor. Images (c) and (d) of case (II) of Fig. 8 show that the film surface deforms replicating the contactor patterns when the viscoelastic film deforms under a physically patterned contactor. The periodicity of the patterns in this simulation is kept at $(\Lambda/4) \times (\Lambda/4)$, while the height of the patterns is fixed at $H_p = 0.03\,H$. The patterns on the contactor surface are decorated in such a manner that the maximum area of contact with the film is $\sim$0.25. Image (d) of Fig. 8 shows that A_r, in this case, has increased about 2.5-fold than case I by using a topographically patterned contactor while T_r reduces to 0.35 [plots (j) and (k) of Fig. 8]. The tapered patterns obtained in the image (d) of Fig. 8 are very commonly observed on the inner tube surface of the carnivorous plant, *Sarracenia leucophylla*, for insect catching [21]. The surfaces consisting of such microstructures also possess high roughness factor (R_f) to become superhydrophobic [77]. A previous work [53] has reported

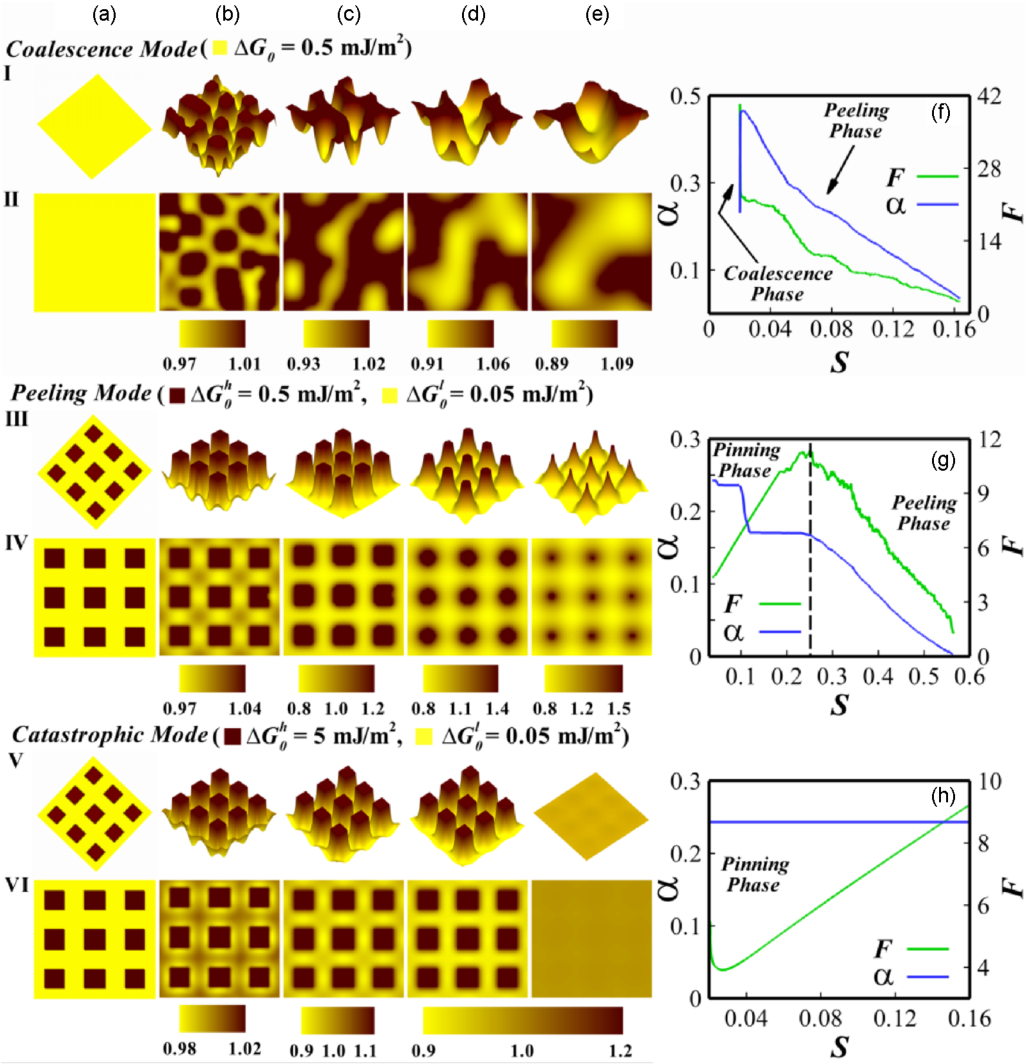

FIG. 7. The nonlinear space-time evolutions of the viscoelastic thin film throughout the changeover of three distinct debonding modes—coalescence, peeling, and catastrophic, in presence of a chemically patterned contactor, in a $3\Lambda \times 3\Lambda$ domain. In the column (a) of rows (I) and (II) the contactor has homogeneous adhesive energy of ΔG_0 while in the rows (III)–(VI) the contactor has dark (light) checkerboard patches with higher (lower) adhesive energy ΔG_0^h (ΔG_0^l). Columns (b)–(e) show the morphological evolution of the free surface at time $T = 0.002, 0.012, 0.05$, and 0.08 for rows (I) and (II), $T = 0.002, 0.02, 0.04$, and 0.05 for rows (III) and (IV), $T = 0.0006, 0.008, 0.01$, and 0.3 for rows (V) and (VI). Rows (I), (III), and (V) [(II), (IV), and (VI)] show the isometric [top] views of the images. Plots (f)–(h) show the variation in α and F with S of the systems shown in the respective rows. Compliance ratio is kept constant at, $C_R = 1.1 \times 10^5$ ($s_e = 15\,\text{nm}$).

that the increase E_C (higher C_R) can improve S_p further, which are perhaps other ways to develop patterns with even higher aspect ratios than the same obtained in the case (II).

In case (III) of Fig. 8 the film is made elastically more compliant (higher E_c) than the previous cases while other particulars remain same as in the case (II) of Fig. 8. Consequently, images (e) and (f) of Fig. 8 show that A_r improves around threefold than the microstructures obtained using homogeneous contactor in case I [plot (j)] of Fig. 8. In such a scenario, the aspect ratio can also be

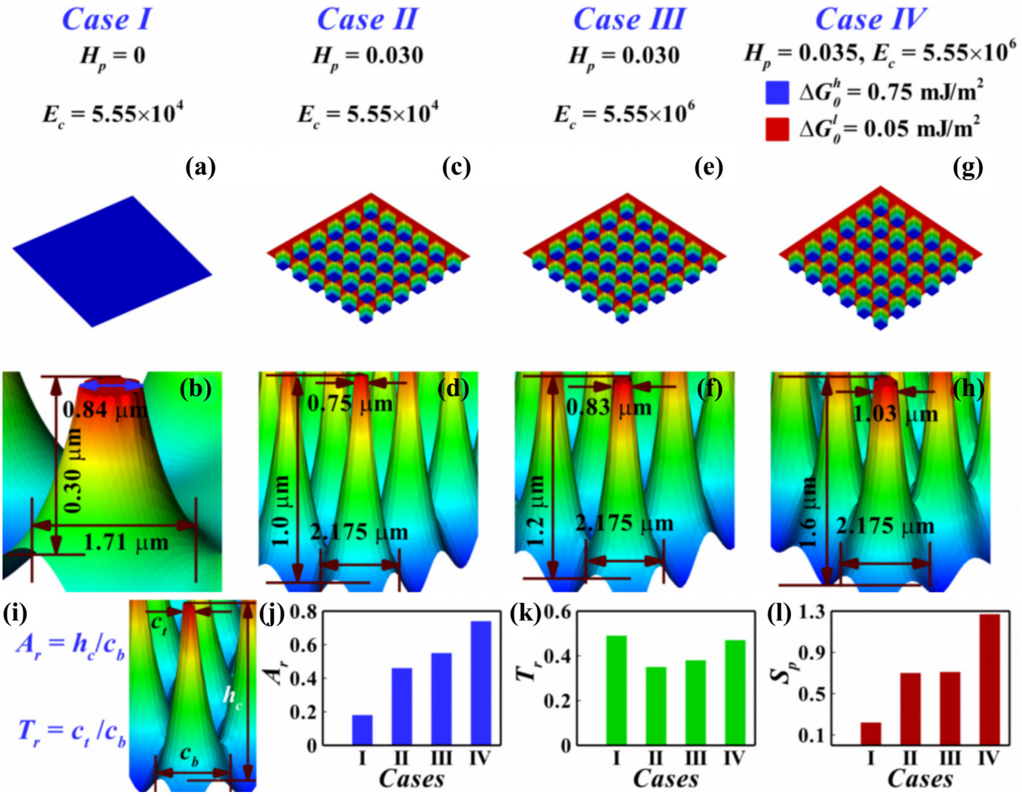

FIG. 8. Example cases of spatiotemporal evolutions of viscoelastic thin film to achieve higher aspect ratio microstructures by altering contactor property, geometry, and C_R, in a $3\Lambda \times 3\Lambda$ domain. Contactor geometries are shown in the images at (a), (c), (e), and (g) while images at (b), (d), (f), and (h) show the dimensions of final microstructures obtained after debonding cycle at time $T = 0.2$ for case (I); $T = 0.7$ for case (II); $T = 0.007$ for case (III); and $T = 0.01$ for case (IV). The parameter, $\mu = 10$ Pa, is used for cases (III) and (IV). Other necessary dimensional parameters for the simulations are listed in Table I. The parameter Λ is kept constant for all the cases. The plot (i) shows the procedure to calculate the aspect ratio (A_r) and the taper ratio (T_r) of the thin film microstructures and introduces some of the relevant dimensional variables like height (h_c), base (c_b), and top (c_t) dimensions of the structures. The plots (j)–(l) show the variation of A_r, T_r, and S_p, respectively, for all the four cases.

improved further by the use of chemical patches on the topographically patterned surface, as shown in the images (g) and (h) of case (IV) of Fig. 8. Image (g) of Fig. 8 shows the physicochemical patch consisting, $\Delta G_0^h = 0.75\,\mathrm{mJ/m^2}$, in the protruded regions of the contactor ($H_p = 0.035\,H$), while the surrounding of the same has $\Delta G_0^l = 0.05\,\mathrm{mJ/m^2}$. In summary, Fig. 8 presents a few example cases where the physicochemical patterns on the contactor help in improving the A_r about fourfold [plot (j) of Fig. 8] and S_p by about sixfold [plot (l) of Fig. 8] when the T_r is maintained between 0.4 and 0.5 [plot (k) of Fig. 8].

Figure 9 shows three different cases where pattern induced contact instability is used to fabricate nanostructures employing the physicochemically patterned contactors. Case (I) shows the formation of nanostructures using the submicron-sized square patterns $[(\Lambda/16) \times (\Lambda/16)]$ with pattern height, $H_p = 0.035\,H$ on the contactor [image (a) of Fig. 9]. In these simulations, the physicochemical patches with higher adhesive energy ($\Delta G_0^h = 0.75\,\mathrm{mJ/m^2}$) have been employed in the protruded regions of the contactor for the elastically more compliant films to develop higher aspect ratio patterns. Image (b) of Fig. 9 confirms that indeed the film surface is capable of producing the

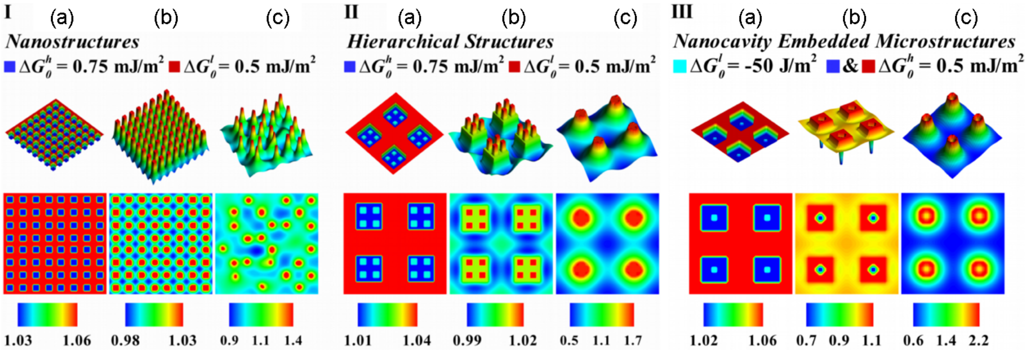

FIG. 9. Fabrication of nano- and multiscale composite structures using spatiotemporal evolutions (3D) of the viscoelastic thin film in the presence of patterned contactors of different geometries and chemical patches in a $\Lambda \times \Lambda$ domain for cases (I)–(III). Column (a) depicts the contactor geometries while columns (b) and (c), respectively, show the final structures of the thin film after the adhesion and debonding cycle at time $T = 0.0002$ and 0.004 for case (I); $T = 0.004$ and 0.23 for case (II); and $T = 0.006$ and 0.12 for case (III). The parameters, for case (I), $\mu = 10$ Pa and $s_e = 60$ nm; for case (II), $s_e = 40$ nm; for case (III), $\mu = 10^2$ Pa and $s_e = 60$ nm. Λ is kept constant for all the cases. Other necessary dimensional parameters are shown in Table I.

nanoridges replicating the checkerboard patterns decorated on the contactor during the adhesion cycle. However, during the debonding phase, the number density reduces, which leaves a few columnar nanostructures to turn into the higher aspect ratio ones before snapping off, as shown in images (c) of Fig. 9. The simulations suggest that in this case, the nanoscale columns can have an aspect ratio as high as, $A_r \approx 1.4$.

Case (II) shows that the use of physicochemically patterned contactors [image (a) of Fig. 9] can also lead to hierarchical structures. In this instance, the dimension of each bigger square patterns on the contactor is $(\Lambda/4) \times (\Lambda/4)$ and the heights of the patterns are $H_p = 0.035\,H$, as shown in the image (a) of Fig. 9. To develop the physicochemically patterned contactor, the protruded bigger square regions (darker blue shade) of the contactor have chemical patches where $\Delta G_0^h = 0.75\,\mathrm{mJ/m^2}$, whereas the smaller squares cavities (lighter blue shade) are of 0.01 H deep, $\Delta G_0^h = 0.75\,\mathrm{mJ/m^2}$, and dimension $(\Lambda/16) \times (\Lambda/16)$. In the presence of such a contactor, the film surface deforms into hierarchical patterns during the adhesion cycle, as shown in images (b) of Fig. 9. The hierarchical structure thus developed is composed of four nanopillars on each micropillar, which can be employed for making the surfaces superhydrophobic. For example, the "lotus effect" [19] on the Lotus (*Nelumbo nucifera*) or Taro (*Colocasia esculenta*) leaves deploy such structures to make the leaf surface superhydrophobic as well as self-cleaning. It may be noted here that although the structures formed during adhesion cycle have a lower aspect ratio, the same can be increased during debonding cycle. The situations shown in the simulations can also be replicated experimentally because the ECL patterns fabricated on the polymers like polydimethylsiloxane (PDMS) can be frozen at any stage of the debonding [images (c) of Fig. 9] by crosslinking with UV exposure [38,78].

Case (III) shows deeply penetrated holes with higher aspect ratio can also be fabricated using the physicochemically patterned contactors. Images (a) of Fig. 9 show the contactor design where the dimensions of the bigger squares are same as in case (II), whereas the smaller squares are chemical patches with the repulsive intermolecular potential of $\Delta G_0^l = 50\,\mathrm{J/m^2}$ and the attractive potential for the surrounding is $\Delta G_0^h = 0.5\,\mathrm{mJ/m^2}$. Image (b) shows deep microcavities with lower aspect ratio are formed during the adhesion cycle. However, during the debonding cycle aspect ratio of these features increase [images (c) of Fig. 9]. It may be noted here that the structures shown here are frequently fabricated for the MEMS or lab-on-a-chip applications using other costly fabrication methodologies [79]. Figure 9 shows the potential of the use of ECL to develop such structures with a moving contactor having physicochemically patterned surfaces.

V. CONCLUSIONS

The conditions for replicating the physical, chemical, or physicochemical patterns decorated on a contactor into the free surface of a thin viscoelastic film undergoing contact instability have been theoretically investigated employing the nonlinear simulations. The conclusions are summarized as follows:

(i) Use of homogeneous contactor produces random irregular patterns whereas introduction of patterns in the contactor impose an order on them. The physical or chemical patterns fabricated on the contactor enforce a lateral variation of intermolecular force, which induces the ordering of the patterns formed on the film surface.

(ii) Simulations suggest that different debonding pathways such as peeling, catastrophic, and coalescence can be engendered by simply varying the wettability contrast across the contactor. Experimental works are yet to appear on the conditions for these transitions of the debonding modes with the use of physical or chemical or physicochemical patches for the same [45]. The snap-off distance for the peeling mode of debonding is found to be highest among these modes, which helps in developing the recipes to fabricate higher aspect ratio structures employing the elastic contact lithography.

(iii) The proposed methodology shows about a fourfold increase in the aspect ratio for the microscale patterns than the previously reported works in this domain [53]. The highest aspect ratio obtained for the nanostructures is $A_r \approx 1.4$, which is remarkably higher than any previous reports on the ECL induced pattern formation.

(iv) Pathways to form nanostructures or hierarchical patterns with significantly higher aspect ratio and density have also been revealed. The simulations show the conditions to generate a host of technologically important structures such as an array or microcolumns or microchannels, high-density nanopillars on microscale columns, high aspect ratio and high-density nanoscale pillars, and microscale columns decorated with cavities or protrusions, among others.

ACKNOWLEDGMENTS

We are thankful for the support from MeitY Grant No. 5(9)/2012-NANO, DST-FIST Grant No. SR/FST/ETII-028/2010, Government of India, and HPC cluster facility of Computer center at IIT Kanpur for financial and technical aids.

APPENDIX A

Parabolic profiles for u and v are assumed as shown in the Eqs. (15) and (16). The expressions of these variables are substituted in the mass conservation Eq. (11) to obtain the following expression of w:

$$w = -\left[\frac{\partial c_1}{\partial x}\frac{z^3}{3} + \frac{\partial c_2}{\partial x}\frac{z^2}{2} + \frac{\partial c_3}{\partial x}z + \frac{\partial c_4}{\partial y}\frac{z^3}{3} + \frac{\partial c_5}{\partial y}\frac{z^2}{2} + \frac{\partial c_6}{\partial y}z + c_7\right]. \tag{A1}$$

Here, c_7 is the integration constant. The expressions of the x-, y-, and z-directional displacements are replaced in the kinematic Eq. (21) to obtain the free surface evolution equation as

$$\frac{\partial h}{\partial t} + \frac{\partial}{\partial x}\left(\frac{\partial c_1}{\partial t}\frac{h^3}{3} + \frac{\partial c_2}{\partial t}\frac{h^2}{2} + \frac{\partial c_3}{\partial t}h\right) + \frac{\partial}{\partial y}\left(\frac{\partial c_4}{\partial t}\frac{h^3}{3} + \frac{\partial c_5}{\partial t}\frac{h^2}{2} + \frac{\partial c_6}{\partial t}h\right) + \frac{\partial c_7}{\partial t} = 0. \tag{A2}$$

The constants c_3, c_6, and c_7 are evaluated using the no-slip and the impermeability boundary conditions [Eqs. (17) and (18)] as

$$c_3 = c_6 = c_7 = 0. \tag{A3}$$

Replacing the expressions of the variables u and v [Eqs. (15) and (16)] in the x- and y-directional equations of motion [Eqs. (12) and (13)], we obtain the expressions of c_1 and c_4 as

$$\eta\dot{c}_1 - (0.5p_x - \mu c_1) = 0, \quad \eta\dot{c}_4 - (0.5p_y - \mu c_4) = 0. \tag{A4}$$

Similarly, using the expressions of the same displacement components in the shear stress balances [Eq. (20)], we get the expressions of c_2 and c_5 as

$$\eta\dot{c}_2 + (hp_x + \mu c_2), \quad \eta\dot{c}_5 + (hp_y + \mu c_5) = 0. \tag{A5}$$

The above expressions of the variables, c_1, c_2, c_4, and c_5 in the free surface evolution equation [Eq. (A2)] lead to the following expression:

$$\frac{\partial h}{\partial t} - \frac{1}{\eta}\left(\frac{\partial}{\partial x}\left(\frac{h^3}{3}\frac{\partial p}{\partial x} + \frac{h^3}{3}(\mu c_1) + \frac{h^2}{2}(\mu c_2)\right) + \frac{\partial}{\partial y}\left(\frac{h^3}{3}\frac{\partial p}{\partial y} + \frac{h^3}{3}(\mu c_4) + \frac{h^2}{2}(\mu c_5)\right)\right) = 0, \tag{A6}$$

where, p is derived by replacing the disjoining pressure, π, from the Eq. (8) into the normal stress balance [Eq. 19] as

$$p = -\frac{1}{6\pi}\left(\frac{A_1}{(d - h_p\psi - h)^3} - \frac{A_2}{h^3} - \frac{3B}{(d - h_p\psi - h)^4}\right) - \gamma\left(\frac{\partial^2 h}{\partial x^2} + \frac{\partial^2 h}{\partial y^2}\right). \tag{A7}$$

APPENDIX B

In this section, we have shown the steps to derive the thin film equation involving the incompressible neo-Hookean viscoelastic materials [72,74] instead of zero-frequency linear viscoelastic material. For this purpose, the reference frame for the particle at time $t = 0$ is considered as $X\{X, Y, Z\}$ and the position of the particle at the given time t is $\mathbf{x}\{x, y, z\}$. Here, $\mathbf{x}$ represents the same three-dimensional (3D) Cartesian coordinate system, as previously shown in the schematic diagram Fig. 1. The displacement of the particle from the reference position at time t is $\mathbf{u}(\mathbf{X}, t) = \mathbf{x}(\mathbf{X}, t) - \mathbf{X}$, where the symbol $\mathbf{u}\{u, v, w\}$ represents the displacement vector and $\mathbf{x}(\mathbf{X}, t)$ represents the motion of a particle in the continuum. The deformation gradient for the Lagrangian formulation is defined as $\mathbf{F} = \partial\mathbf{x}/\partial\mathbf{X}$. The constitutive relation of a neo-Hookean solid with viscous dissipation in the Lagrangian framework is expressed as [73,75,76],

$$\boldsymbol{\sigma} = -p_f\mathbf{I} + \mu(\mathbf{F}\cdot\mathbf{F}^{\mathrm{T}}) + \eta(\mathbf{L} + \mathbf{L}^{\mathrm{T}}), \tag{B1}$$

where $\boldsymbol{\sigma}$ is the Cauchy stress tensor. The spatial strain rate tensor, $\mathbf{L}$, is defined as, $\mathbf{L} = \dot{\mathbf{F}}\cdot\mathbf{F}^{-1}$ in which the overdot represents the time derivative. To keep the parity in the formulation presented in the main manuscript, the following formulation is presented in the Eulerian framework, wherein the deformation gradient is defined as $\mathbf{f} = \partial\mathbf{X}/\partial\mathbf{x}$, wherein $\mathbf{F} = \mathbf{f}^{-1}$ by definition. This relation is utilized to convert the Lagrangian constitutive relation Eq. (B1) into a Eulerian constitutive relation as [76]

$$\boldsymbol{\sigma} = -p_f\mathbf{I} + \mu(\mathbf{f}^{\mathrm{T}}\cdot\mathbf{f})^{-1} + \eta(\dot{\mathbf{f}}^{-1}\cdot\mathbf{f} + (\dot{\mathbf{f}}^{-1}\cdot\mathbf{f})^{\mathrm{T}}). \tag{B2}$$

The deformation gradient can also be expressed as $\mathbf{f} = \partial(\mathbf{x} - \mathbf{u})/\partial\mathbf{x} = \mathbf{I} - \nabla\mathbf{u}$. The dynamics of such incompressible neo-Hookean solid film under the influence of an approaching contactor can be described using the incompressibility condition together with the equation of motion as

$$\operatorname{Det}\mathbf{f} = 1, \tag{B3}$$

$$\nabla\cdot\boldsymbol{\sigma} + \boldsymbol{\Pi}_{\mathbf{v}} = 0. \tag{B4}$$

Here, $\mathbf{\Pi_v}$ is the van der Waals body force term which can be expressed in terms of π. No-slip and impermeability boundary conditions are enforced at the substrate-film interface ($z = 0$),

$$\mathbf{u} = \dot{\mathbf{u}} = 0. \tag{B5}$$

At the film-air interface ($z = h(x,y,t)$), we have enforced the normal and tangential stress balances, and the kinematic condition as boundary conditions,

$$\mathbf{n} \cdot \boldsymbol{\sigma} \cdot \mathbf{n} = -\gamma\kappa, \tag{B6}$$

$$\mathbf{n} \cdot \boldsymbol{\sigma} \cdot \mathbf{t} = 0, \tag{B7}$$

$$DQ/Dt = \dot{Q} + \dot{\mathbf{u}} \cdot \nabla Q = 0, \tag{B8}$$

where $Q(=z - h(x,y,t))$ defines the free surface of the thin film and D/Dt represents material derivative. The governing equations [Eqs. (B3) and (B4)] and the boundary conditions [Eqs. (B5)–(B8)] transform into the following:

$$\begin{aligned} &u_{,x} + v_{,y} + w_{,z} - v_{,y}w_{,z} + w_{,y}v_{,z} - u_{,x}w_{,z} - u_{,x}v_{,y} + v_{,x}u_{,y} + w_{,x}u_{,z} \\ &\quad + u_{,x}v_{,y}w_{,z} - u_{,x}w_{,y}v_{,z} - v_{,x}u_{,y}w_{,z} + v_{,x}w_{,y}u_{,z} + w_{,x}u_{,y}v_{,z} - w_{,x}v_{,y}u_{,z} = 0, \end{aligned} \tag{B9}$$

$$\begin{aligned} \sigma_{xx,x} + \sigma_{xy,y} + \sigma_{xz,z} + \pi_{,x} &= 0, \\ \sigma_{yx,x} + \sigma_{yy,y} + \sigma_{yz,z} + \pi_{,y} &= 0, \\ \sigma_{zx,x} + \sigma_{zy,y} + \sigma_{zz,z} + \pi_{,z} &= 0; \end{aligned} \tag{B10}$$

$$u = v = 0, \quad w = 0; \tag{B11}$$

$$\begin{aligned} &\left(\frac{h_{,x}^2}{1+h_{,x}^2+h_{,y}^2}\sigma_{xx} + \frac{h_{,x}h_{,y}}{1+h_{,x}^2+h_{,y}^2}\sigma_{xy} - \frac{h_{,x}}{1+h_{,x}^2+h_{,y}^2}\sigma_{xz}\right) \\ &\quad + \left(\frac{h_{,x}h_{,y}}{1+h_{,x}^2+h_{,y}^2}\sigma_{yx} + \frac{h_{,y}^2}{1+h_{,x}^2+h_{,y}^2}\sigma_{yy} - \frac{h_{,y}}{1+h_{,x}^2+h_{,y}^2}\sigma_{yz}\right) \\ &\quad + \left(-\frac{h_{,x}}{1+h_{,x}^2+h_{,y}^2}\sigma_{zx} - \frac{h_{,y}}{1+h_{,x}^2+h_{,y}^2}\sigma_{zy} + \frac{1}{1+h_{,x}^2+h_{,y}^2}\sigma_{zz}\right) = \gamma(\nabla \cdot \mathbf{n}), \end{aligned} \tag{B12}$$

$$\begin{aligned} &\left(\frac{h_{,x}}{1+h_{,x}^2+h_{,y}^2}\sigma_{xx} + \frac{h_{,y}}{1+h_{,x}^2+h_{,y}^2}\sigma_{xy} - \frac{1}{1+h_{,x}^2+h_{,y}^2}\sigma_{xz}\right) \\ &\quad + \left(\frac{h_{,x}^2}{1+h_{,x}^2+h_{,y}^2}\sigma_{zx} + \frac{h_{,x}h_{,y}}{1+h_{,x}^2+h_{,y}^2}\sigma_{zy} - \frac{h_{,x}}{1+h_{,x}^2+h_{,y}^2}\sigma_{zz}\right) = 0, \end{aligned} \tag{B13}$$

$$\begin{aligned} &\left(\frac{h_{,x}}{1+h_{,x}^2+h_{,y}^2}\sigma_{yx} + \frac{h_{,y}}{1+h_{,x}^2+h_{,y}^2}\sigma_{yy} - \frac{1}{1+h_{,x}^2+h_{,y}^2}\sigma_{yz}\right) \\ &\quad + \left(\frac{h_{,x}h_{,y}}{1+h_{,x}^2+h_{,y}^2}\sigma_{zx} + \frac{h_{,y}^2}{1+h_{,x}^2+h_{,y}^2}\sigma_{zy} - \frac{h_{,y}}{1+h_{,x}^2+h_{,y}^2}\sigma_{zz}\right) = 0, \end{aligned} \tag{B14}$$

$$\dot{h} + \dot{u}h_{,x} + \dot{v}h_{,y} = \dot{w}. \tag{B15}$$

The variables with subscript preceded by a comma denote partial differentiation with respect to the subscripted variable expressions.

1. Long-wave analysis

The spatiotemporal evolution equation for the deforming free surface of the thin film is theoretically modeled in the long-wave limit. In this limit, the Cauchy stress tensor reduced to

$$\boldsymbol{\sigma} = -p_f\begin{pmatrix}1 & 0 & 0\\ 0 & 1 & 0\\ 0 & 0 & 1\end{pmatrix} + \mu\begin{pmatrix}1 & 0 & u_{,z}\\ 0 & 1 & v_{,z}\\ u_{,z} & v_{,z} & 1\end{pmatrix} + \eta\left(\frac{\partial}{\partial t}\begin{pmatrix}0 & 0 & 0\\ 0 & 0 & 0\\ u_{,z} & v_{,z} & 0\end{pmatrix} + \frac{\partial}{\partial t}\begin{pmatrix}0 & 0 & u_{,z}\\ 0 & 0 & v_{,z}\\ 0 & 0 & 0\end{pmatrix}\right). \tag{B16}$$

The simplified continuity and momentum equations are obtained as

$$u_{,x} + v_{,y} + w_{,z} = 0, \tag{B17}$$

$$\mu u_{,zz} + \eta \dot{u}_{,zz} = p_{,x}, \tag{B18}$$

$$\mu v_{,zz} + \eta \dot{v}_{,zz} = p_{,y}, \tag{B19}$$

$$p_{,z} = 0. \tag{B20}$$

The no-slip and impermeability boundary conditions in the long-wave limit remain same as Eq. (B11). The stress balances [Eqs. (B12)–(B14)] reduce to

$$p + \pi + \gamma(h_{,xx} + h_{,yy}) = 0, \tag{B21}$$

$$\mu u_{,z} + \eta \dot{u}_{,z} = 0, \tag{B22}$$

$$\mu v_{,z} + \eta \dot{v}_{,z} = 0. \tag{B23}$$

The kinematic condition also remains same as Eq. (B15). The obtained set of governing equations [Eqs. (B17)–(B20)] and boundary conditions [Eqs. (B11), (B21)–(B23), (B15)] are exactly similar to the ones that are obtained for a linear viscoelastic solid [Eqs. (11)–(14), (17)–(21)] in the main manuscript. Following the procedure presented in Sec. IIB, we end up with the same set of evolution equations [Eqs. (22)–(25)] similar to the linear viscoelastic thin film, as shown in the main manuscript.

---

[1] A. Rehman and S. Lee, Review of the potential of the Ni/Cu plating technique for crystalline silicon solar cells, Materials **7**, 1318 (2014).

[2] A. N. Gent and R. P. Petrich, Adhesion of viscoelastic materials to rigid substrates, Proc. R. Soc. London, Ser. A **310**, 433 (1969).

[3] C. Gay and L. Leibler, Theory of Tackiness, Phys. Rev. Lett. **82**, 936 (1999).

[4] Y. Y. Lin, C. Y. Hui, and H. D. Conway, A detailed elastic analysis of the flat punch (tack) test for pressure-sensitive adhesives, J. Polym. Sci., Part B: Polym. Phys. **38**, 2769 (2000).

[5] A. J. Crosby, K. R. Shull, H. Lakrout, and C. Creton, Deformation and failure modes of adhesively bonded elastic layers, J. Appl. Phys. **88**, 2956 (2000).

[6] I. Chikina and C. Gay, Cavitation in Adhesives, Phys. Rev. Lett. **85**, 4546 (2000).

[7] C. Creton, J. Hooker, and K. R. Shull, Bulk and interfacial contributions to the debonding mechanisms of soft adhesives: Extension to large strains, Langmuir **17**, 4948 (2001).

[8] K. Brown, J. C. Hooker, and C. Creton, Micromechanisms of tack of soft adhesives based on styrenic block copolymers, Macromol. Mater. Eng. **287**, 163 (2002).

[9] M. T. Northen and K. L. Turner, A batch fabricated biomimetic dry adhesive, Nanotechnology **16**, 1159 (2005).

[10] L. F. Boesel, C. Greiner, E. Arzt, and A. del Campo, Gecko-inspired surfaces: A path to strong and reversible dry adhesives, Adv. Mater. **22**, 2125 (2010).

[11] A. Majumder, A. Ghatak, and A. Sharma, Microfluidic adhesion induced by subsurface microstructures, Science **318**, 258 (2007).

[12] A. del Campo and E. Arzt, Fabrication approaches for generating complex micro- and nanopatterns on polymeric surfaces, Chem. Rev. **108**, 911 (2008).

[13] B. Bhushan, Nanotribology and nanomechanics of MEMS/NEMS and BioMEMS/BioNEMS materials and devices, Microelectron. Eng. **84**, 387 (2007).

[14] G. Chen, G. T. McCandless, R. L. McCarley, and S. A. Soper, Integration of large-area polymer nanopillar arrays into microfluidic devices using in situ polymerization cast molding, Lab Chip **7**, 1424 (2007).

[15] Z.-F. Li, H. Zhang, Q. Liu, Y. Liu, L. Stanciu, and J. Xie, Hierarchical nanocomposites of vanadium oxide thin film anchored on graphene as high-performance cathodes in Li-ion batteries, ACS Appl. Mater. Interfaces **6**, 18894 (2014).

[16] Z. Nie and E. Kumacheva, Patterning surfaces with functional polymers, Nat. Mater. **7**, 277 (2008).

[17] C. Tan, Z. Liu, W. Huang, and H. Zhang, Non-volatile resistive memory devices based on solution-processed ultrathin two-dimensional nanomaterials, Chem. Soc. Rev. **44**, 2615 (2015).

[18] M. Nosonovsky and B. Bhushan, Multiscale effects and capillary interactions in functional biomimetic surfaces for energy conversion and green engineering, Philos. Trans. R. Soc., A **367**, 1511 (2009).

[19] K. Koch, B. Bhushan, Y. C. Jung, and W. Barthlott, Fabrication of artificial Lotus leaves and significance of hierarchical structure for superhydrophobicity and low adhesion, Soft Matter **5**, 1386 (2009).

[20] Y. Si and Z. Guo, Superhydrophobic nanocoatings: From materials to fabrications and to applications, Nanoscale **7**, 5922 (2015).

[21] K. Koch, B. Bhushan, and W. Barthlott, Diversity of structure, morphology and wetting of plant surfaces, Soft Matter **4**, 1943 (2008).

[22] Z. Wang, L. Zhu, W. Li, and H. Liu, Bioinspired in situ growth of conversion films with underwater superoleophobicity and excellent self-cleaning performance, ACS Appl. Mater. Interfaces **5**, 10904 (2013).

[23] X.-M. Li, D. Reinhoudt, and M. Crego-Calama, What do we need for a superhydrophobic surface? A review on the recent progress in the preparation of superhydrophobic surfaces, Chem. Soc. Rev. **36**, 1350 (2007).

[24] W. Lu and C. M. Lieber, Nanoelectronics from the bottom up, Nat. Mater. **6**, 841 (2007).

[25] B. Guillotin, and F. Guillemot, Cell patterning technologies for organotypic tissue fabrication, Trends Biotechnol. **29**, 183 (2011).

[26] K. Kendall, The adhesion and surface energy of elastic solids, J. Phys. D: Appl. Phys. **4**, 1186 (1971).

[27] S. Herminghaus, Dynamical Instability of Thin Liquid Films Between Conducting Media, Phys. Rev. Lett. **83**, 2359 (1999).

[28] P. Attard, Interaction and deformation of elastic bodies: Origin of adhesion hysteresis, J. Phys. Chem. B **104**, 10635 (2000).

[29] K. R. Shull, C. M. Flanigan, and A. J. Crosby, Fingering Instabilities of Confined Elastic Layers in Tension, Phys. Rev. Lett. **84**, 3057 (2000).

[30] E. Schaffer, T. Thurn-Albrecht, T. P. Russell, and U. Steiner, Electrically induced structure formation and pattern transfer, Nature **403**, 874 (2000).

[31] W. Mönch and S. Herminghaus, Elastic instability of rubber films between solid bodies, Europhys. Lett. **53**, 525 (2001).

[32] C. Q. Ru, Surface wrinkling of two mutually attracting elastic thin films due to van der Waals forces, J. Appl. Phys. **90**, 6098 (2001).

[33] V. Shenoy and A. Sharma, Pattern Formation in a Thin Solid Film with Interactions, Phys. Rev. Lett. **86**, 119 (2001).

[34] V. Shenoy and A. Sharma, Stability of a thin elastic film interacting with a contactor, J. Mech. Phys. Solids **50**, 1155 (2002).

[35] A. Ghatak and M. K. Chaudhury, Adhesion-induced instability patterns in thin confined elastic film, Langmuir **19**, 2621 (2003).

[36] A. Ghatak, L. Mahadevan, J. Y. Chung, M. K. Chaudhury, and V. Shenoy, Peeling from a biomimetically patterned thin elastic film, Proc. R. Soc. London, Ser. A **460**, 2725 (2004).

[37] H. Tian, J. Shao, H. Hu, L. Wang, and Y. Ding, Generation of hierarchically ordered structures on a polymer film by electrohydrodynamic structure formation, ACS Appl. Mater. Interfaces **8**, 16419 (2016).

[38] M. Gonuguntla, A. Sharma, J. Sarkar, S. A. Subramanian, M. Ghosh, and V. Shenoy, Contact Instability in Adhesion and Debonding of Thin Elastic Films, Phys. Rev. Lett. **97**, 018303 (2006).

[39] A. Ghatak, M. K. Chaudhury, V. Shenoy, and A. Sharma, Meniscus Instability in a Thin Elastic Film, Phys. Rev. Lett. **85**, 4329 (2000).

[40] R. Mukherjee and A. Sharma, Creating self-organized submicrometer contact instability patterns in soft elastic bilayers with a topographically patterned stamp, ACS Appl. Mater. Interfaces **4**, 355 (2012).

[41] J. Nase, A. Lindner, and C. Creton, Pattern Formation During Deformation of a Confined Viscoelastic Layer: From a Viscous Liquid to a Soft Elastic Solid, Phys. Rev. Lett. **101**, 074503 (2008).

[42] D. Martina, C. Creton, P. Damman, M. Jeusette, and A. Lindner, Adhesion of soft viscoelastic adhesives on periodic rough surfaces, Soft Matter **8**, 5350 (2012).

[43] F. Tanguy, M. Nicoli, A. Lindner, and C. Creton, Quantitative analysis of the debonding structure of soft adhesives, Eur. Phys. J. E **37**, 3 (2014).

[44] R. Mukherjee, R. C. Pangule, A. Sharma, and I. Banerjee, Contact instability of thin elastic films on patterned substrates, J. Chem. Phys. **127**, 064703 (2007).

[45] N. Bhandaru, A. Sharma, and R. Mukherjee, Programmable nanopatterns by controlled debonding of soft elastic films, ACS Appl. Mater. Interfaces **9**, 19409 (2017).

[46] J. Sarkar, A. Sharma, and V. Shenoy, Adhesion and debonding of soft elastic films on rough and patterned surfaces, J. Adhes. **81**, 271 (2005).

[47] P. D. S. Reddy, D. Bandyopadhyay, and A. Sharma, Self-organized ordered arrays of core−shell columns in viscous bilayers formed by spatially varying electric fields, J. Phys. Chem. C **114**, 21020 (2010).

[48] A. Chakrabarti and M. K. Chaudhury, Direct measurement of the surface tension of a soft elastic hydrogel: Exploration of elastocapillary instability in adhesion, Langmuir **29**, 6926 (2013).

[49] R. Verma, A. Sharma, I. Banerjee, and K. Kargupta, Spinodal instability and pattern formation in thin liquid films confined between two plates, J. Colloid Interface Sci. **296**, 220 (2006).

[50] D. Bandyopadhyay, R. Gulabani, and A. Sharma, Instability and dynamics of thin liquid bilayers, Ind. Eng. Chem. Res. **44**, 1259 (2005).

[51] D. Bandyopadhyay and A. Sharma, Dewetting pathways and morphology of unstable thin liquid bilayers, J. Phys. Chem. B **112**, 11564 (2008).

[52] J. Sarkar, A. Sharma, and V. Shenoy, Adhesion and debonding of soft elastic films: Crack patterns, metastable pathways, and forces, Langmuir **21**, 1457 (2005).

[53] A. Ghosh, D. Bandyopadhyay, and A. Sharma, Influence of the mutable kinetic parameters on the adhesion and debonding of thin viscoelastic films, J. Colloid Interface Sci. **477**, 109 (2016).

[54] J. Wang, M. Tolan, O. H. Seeck, S. K. Sinha, O. Bahr, M. H. Rafailovich, and J. Sokolov, Surfaces of Strongly Confined Polymer Thin Films Studied by X-Ray Scattering, Phys. Rev. Lett. **83**, 564 (1999).

[55] S. Kumar and O. K. Matar, Dewetting of thin liquid films near soft elastomeric layers, J. Colloid Interface Sci. **273**, 581 (2004).

[56] O. K. Matar, V. Gkanis, and S. Kumar, Nonlinear evolution of thin liquid films dewetting near soft elastomeric layers, J. Colloid Interface Sci. **286**, 319 (2005).

[57] A. Patra, D. Bandyopadhyay, G. Tomar, A. Sharma, and G. Biswas, Instability and dewetting of ultrathin solid viscoelastic films on homogeneous and heterogeneous substrates, J. Chem. Phys. **134**, 064705 (2011).

[58] G. H. Fredrickson, A. Ajdari, L. Leibler, and J. P. Carton, Surface modes and deformation energy of a molten polymer brush, Macromolecules **25**, 2882 (1992).

[59] F. Saulnier, T. Ondarçuhu, A. Aradian, and E. Raphaël, Adhesion between a viscoelastic material and a solid Surface, Macromolecules **37**, 1067 (2004).

[60] S. Patil, A. Malasi, A. Majumder, A. Ghatak, and A. Sharma, Reusable antifouling viscoelastic adhesive with an elastic skin, Langmuir **28**, 42 (2012).

[61] H. Lakrout, C. Creton, D. Ahn, and K. R. Shull, Influence of molecular features on the tackiness of acrylic polymer melts, Macromolecules **34**, 7448 (2001).

[62] X. Callies, O. Herscher, C. Fonteneau, A. Robert, S. Pensec, L. Bouteiller, G. Ducouret, and C. Creton, Combined effect of chain extension and supramolecular interactions on rheological and adhesive properties of acrylic pressure-sensitive adhesives, ACS Appl. Mater. Interfaces **8**, 33307 (2016).

[63] R. Gurney, A. Henry, R. Schach, A. Lindner, and C. Creton, Molecular weight dependence of interdiffusion and adhesion of polymers at short contact times, Langmuir **33**, 1670 (2017).

[64] S. Patil, R. Mangal, A. Malasi, and A. Sharma, Biomimetic wet adhesion of viscoelastic liquid films anchored on micropatterned elastic substrates, Langmuir **28**, 14784 (2012).

[65] C. Costantino and C. Matteo, Fracture and adhesion of soft materials: A review, Rep. Prog. Phys. **79**, 046601 (2016).

[66] S. Sun, M. Li, and A. Liu, A review on mechanical properties of pressure sensitive adhesives, Int. J. Adhes. Adhes. **41**, 98 (2013).

[67] A. Lindner, T. Maevis, R. Brummer, B. Lühmann, and C. Creton, Subcritical failure of soft acrylic adhesives under tensile stress, Langmuir **20**, 9156 (2004).

[68] H. Huang, A. Dasgupta, and E. Mirbagheri, Mechanistic model for the mechanical behavior of assemblies bonded with pressure-sensitive adhesives, in *Proceedings of the 2016 17th International Conference on Thermal, Mechanical and Multi-Physics Simulation and Experiments in Microelectronics and Microsystems (EuroSimE)* (IEEE, Montpelier, France, 2016), pp. 1–4.

[69] X. Deng, Progress on rubber-based pressure-sensitive adhesives, J. Adhes. **1** (2016).

[70] F. Deplace, M. A. Rabjohns, T. Yamaguchi, A. B. Foster, C. Carelli, C.-H. Lei, K. Ouzineb, J. L. Keddie, P. A. Lovell, and C. Creton, Deformation and adhesion of a periodic soft-soft nanocomposite designed with structured polymer colloid particles, Soft Matter **5**, 1440 (2009).

[71] F. Deplace, C. Carelli, A. Langenfeld, M. A. Rabjohns, A. B. Foster, P. A. Lovell, and C. Creton, Controlled sparse and percolating cross-linking in waterborne soft adhesives, ACS Appl. Mater. Interfaces **1**, 2021 (2009).

[72] P. Chokshi and V. Kumaran, Weakly nonlinear analysis of viscous instability in flow past a neo-Hookean surface, Phys. Rev. E **77**, 056303 (2008).

[73] Y. Ma and C.-O. Ng, Wave propagation and induced steady streaming in viscous fluid contained in a prestressed viscoelastic tube, Phys. Fluids **21**, 051901 (2009).

[74] V. Shankar, Stability of fluid flow through deformable neo-Hookean tubes, J. Fluid Mech. **627**, 291 (2009).

[75] D. Giribabu and V. Shankar, Consistent formulation of solid dissipative effects in stability analysis of flow past a deformable solid, Phys. Rev. Fluids **1**, 033602 (2016).

[76] R. Patne, D. Giribabu, and V. Shankar, Consistent formulations for stability of fluid flow through deformable channels and tubes, J. Fluid Mech. **827**, 31 (2017).

[77] M. Nosonovsky and B. Bhushan, Roughness-induced superhydrophobicity: A way to design non-adhesive surfaces, J. Phys.: Condens. Matter **20**, 225009 (2008).

[78] N. Bowden, W. T. S. Huck, K. E. Paul, and G. M. Whitesides, The controlled formation of ordered, sinusoidal structures by plasma oxidation of an elastomeric polymer, Appl. Phys. Lett. **75**, 2557 (1999).

[79] B. Wu, A. Kumar, and S. Pamarthy, High aspect ratio silicon etch: A review, J. Appl. Phys. **108**, 051101 (2010).